Biomechanics and Modeling in Mechanobiology (2024) 23:2155–2176
https://doi.org/10.1007/s10237-024-01886-8

ORIGINAL PAPER

A morpho-viscoelasticity theory for growth in proliferating aggregates

Prakhar Bandil[1] · **Franck J. Vernerey**[1]

Received: 6 May 2024 / Accepted: 14 August 2024 / Published online: 2 September 2024

Abstract
Despite significant research efforts in the continuum modeling of biological growth, certain aspects have been overlooked. For instance, numerous investigations have examined the influence of morphogenetic cell behaviors, like division and intercalation, on the mechanical response of passive (non-growing) tissues. Yet, their impact on active growth dynamics remains inadequately explored. A key reason for this inadequacy stems from challenges in the continuum treatment of cell-level processes. While some coarse-grained models have been proposed to address these shortcomings, a focus on cell division and cell expansion has been missing, rendering them unusable when it comes to modeling growth. Moreover, existing studies are limited to two-dimensional tissues and are yet to be formally extended to three-dimensional multicellular systems. To address these limitations, we here present a generalized multiscale model for three-dimensional aggregates that accounts for complex morphogenetic movements that include division, expansion, and intercalation. The proposed continuum theory thus allows for a comprehensive exploration into the growth and dissipation mechanics of proliferating aggregates, such as spheroids and organoids.

Keywords Growth mechanics · Cell division · Cell intercalation · Network remodeling · Transient network theory

1 Introduction

Establishing a precise relationship between mechanical loading and biological response is crucial for understanding various developmental and pathological processes, such as tumor growth (Zhang et al. 2020). Mathematical modeling of growth (volume change) and morphogenesis (shape change) has, therefore, remained a central focus in mechanobiology research (Taber 2020). These models primarily focus on elucidating the coupling between mechanics and the phenomena of growth and morphogenesis. Additionally, they inform the design of innovative experiments for modern tissue and organoid engineering applications (Vernerey et al. 2021), by aiding in predictive modeling and suggesting plausible mechanisms responsible for a specific response. Researchers have thus developed numerous theoretical and computational modeling tools aimed at predicting the emergent dynamics of developing tissues under diverse chemical and mechanical factors. These models can broadly be classified based on whether the growing body is considered as a continuum object or as a collection of individual cells.

On the continuum front, one of the most prominent theories for modeling volumetric growth in soft biological materials is the theory of finite kinematic growth, also referred to as *morphoelasticity* (Goriely 2017). Since its advent, the morphoelasticity theory has been applied extensively to study several growth-related phenomena (Kuhl 2014). Some examples include growth-induced residual stresses (Ambrosi and Mollica 2002), stress-modulated growth (Ambrosi and Mollica 2004), and tumor morphogenesis (Mills et al. 2014). Morphoelasticity theory uses a single second-order tensorial variable, called the growth tensor, to phenomenologically model macroscopic tissue growth (Rodriguez et al. 1994). In reality, however, growth and morphogenesis are mediated at the cellular (and even subcellular) level via multiple morphogenetic processes like expansion, division, intercalation, and apoptosis. The inability to—capture the macroscopic influence of these microscopic events and relate the growth tensor to driving mechanisms—is the main limitation of morphoelasticity theory (Ambrosi et al. 2011; Jones and Chapman 2012).

In this regard, agent-based models (Van Liedekerke et al. 2015), which consider individual cells, help us understand

✉ Franck J. Vernerey
franck.vernerey@colorado.edu

[1] Department of Mechanical Engineering, University of Colorado, Boulder, USA

how cellular activities manifest globally and drive the emergent collective response. For example, vertex- (Lin et al. 2017) and Voronoi- (Barton et al. 2017) model-based simulations have demonstrated the role of cell–cell interactions in growing epithelial monolayers. The proficiency of these models lies in their ability to encompass not only cellular morphogenetic processes but also cellular properties such as stiffness, contractility, and adhesion to name a few. As a result, the tissue description provided by these discrete methods bears a closer resemblance to biology. Nevertheless, even such techniques are not without flaws, with the main challenges being the extension to three-dimensional complex geometries and the high computational costs involved.

This led to several efforts to unify the continuous and discrete approaches, intending to develop computationally tractable models that can also preserve some cell-level information. Researchers have been able to mechanistically incorporate cell-scale behavior to model tissue elasticity (Staddon et al. 2023; Brodland et al. 2006) and cell rearrangements owing to intercalation (Ishihara et al. 2017) within continuous frameworks. To bridge the cell- and tissue scale behaviors, these models follow a coarse-grained technique (Graner et al. 2008) wherein the effective response at the tissue scale is derived in an averaged sense from the individual response of constituent cells. While the mathematical formulation employed for coarse-graining in these studies is extendable to three dimensions, the primary focus, to this date, has been on two-dimensional cell monolayers like epithelial tissues. Furthermore, the phenomenon of growth which involves cell expansion and division (termed together as *proliferation*) has garnered even less attention.

This sets the objective for the current study—to address the shortcomings of existing continuum theories and propose a multiscale modeling framework that comprehensively models population growth dynamics. The goal is to refine the coarse-grained models with mechanisms like proliferation that hold significance to the growth phenomenon. Though some authors have opted for a more computational approach (Lejeune and Linder 2017) to achieve this, we here are interested in introducing a theoretical tool that can be implemented using nonlinear finite element analysis (FEA), similar to morphoelasticity. The presented theory is an extension of our previous work (Bandil and Vernerey 2023) on confluent cell monolayers that laid down the fundamental ideas regarding the multiscale modeling of cellular processes. Here, we not only expand those ideas to three-dimensional cell ensembles or *aggregates* but also offer novel interpretations of cellular processes-induced inelastic deformation.

The article is organized as follows. In Sec. 2, we start by providing a concise overview of the classical morphoelasticity theory. Subsequently, we discuss the need to generalize the conventional theory to *morpho-viscoelasticity* that accounts for the elasto-visco-plastic behavior of cell aggregates. Section 3 delves into the development of morpho-viscoelasticity theory. For this, we employ transient network theory (TNT) (Vernerey et al. 2017)—a versatile framework that has been used to study viscoelasticity due to dynamic networks across various systems including plant cell walls (Lalitha Sridhar et al. 2018), fire ant aggregations (Vernerey et al. 2018), hydrogels (Crespo-Cuevas et al. 2023), and cell monolayers (Bandil and Vernerey 2023). This section discusses the details of the mathematical modeling of elastic and inelastic deformation in the aggregate. In Sec. 4, we illustrate the developed theory, through simple case studies focusing on the mechanics of proliferation and intercalation. In particular, we look at how cellular processes control the macroscopic stress state and deformation within a growing aggregate. Finally, Sec. 5 offers concluding remarks concerning the study's limitations and identifies open issues for future research.

2 Background

2.1 Morphoelasticity

Morphoelasticity theory is based on the notion of multiple natural configurations, initially proposed to study finite inelastic deformations in solids (Rajagopal 1995). In the context of growth, the idea is summarized as follows.

Kinematics. Consider an arbitrary point $\mathcal{P}$ inside a continuum body in its *initial* (undeformed) configuration $\mathcal{B}_0$. Let $\boldsymbol{X}$ be the Lagrangian coordinate of $\mathcal{P} \in \mathcal{B}_0$ in a three-dimensional Euclidean space with basis $\boldsymbol{e}_a, (a = 1, 2, 3)$, as indicated in Fig. 1. As the body moves in space with time, its configuration at any time t is given by $\mathcal{B}(t)$, which is called the *current* configuration. During this motion, each point $\mathcal{P} \in \mathcal{B}_0$ with position vector $\boldsymbol{X}$ gets mapped, with one-to-one and onto correspondence, to its current position in $\mathcal{B}(t)$, where the current position is identified by its spatial coordinate $\boldsymbol{x}(\boldsymbol{X}, t)$ (see Fig. 1). The tangent mapping from $\mathcal{B}_0$ to $\mathcal{B}(t)$ is then described by the deformation gradient tensor $\boldsymbol{F}(\boldsymbol{X}, t)$, defined as:

$$\boldsymbol{F} := \frac{\partial \boldsymbol{x}}{\partial \boldsymbol{X}} \tag{1}$$

As per morphoelasticity, the deformation gradient $\boldsymbol{F}$ can be multiplicatively decomposed into an elastic component $\boldsymbol{F}_e$ and a growth component $\boldsymbol{F}_g$ as (Rodriguez et al. (1994); Lubarda and Hoger (2002)):

$$\boldsymbol{F} = \boldsymbol{F}_e \boldsymbol{F}_g \tag{2}$$

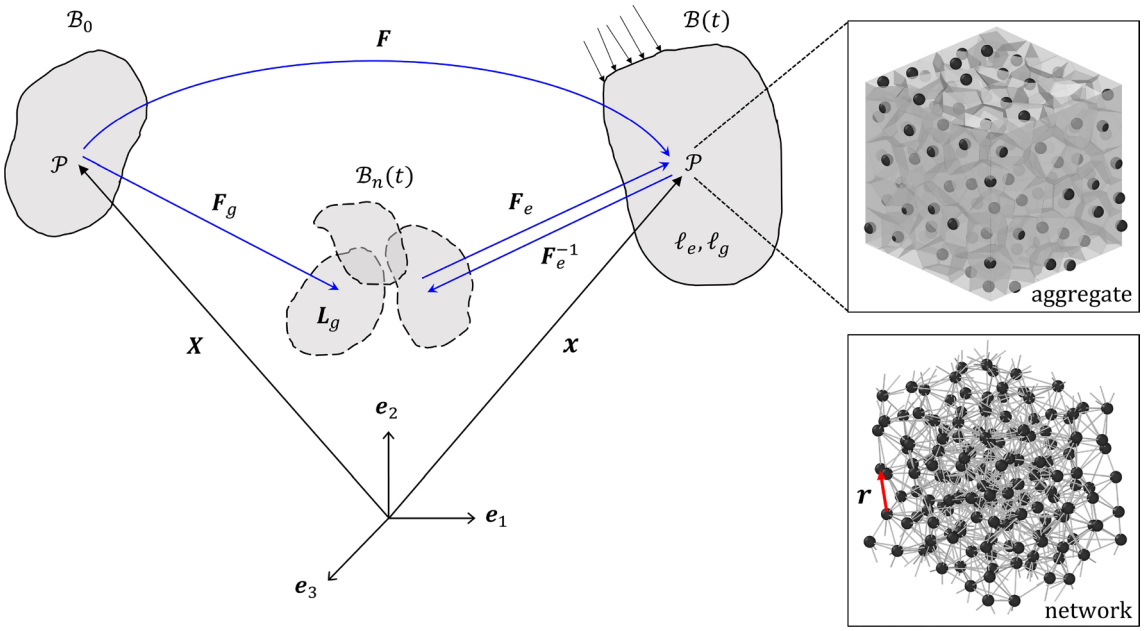

Fig. 1 Illustration of different frames as per morphoelasticity theory. Also shown is a cell aggregate and its corresponding network of segment vectors $\boldsymbol{r}$ embedded within point $\mathcal{P} \in \mathcal{B}(t)$

Accordingly, the Jacobian of deformation, given by $J = \det \boldsymbol{F}$, follows the split $J = J_e J_g$, where $J_e = \det \boldsymbol{F}_e$ and $J_g = \det \boldsymbol{F}_g$ represent, respectively, the volumetric changes due to elastic and growth-induced inelastic deformations. Upon unloading the current state *elastically* (i.e., described by mapping operator $\boldsymbol{F}_e^{-1}$), a *fictitious* configuration, denoted by $\mathcal{B}_n(t)$, is obtained (see Fig. 1). This *intermediate* stress-free configuration differs from the initial stress-free configuration $\mathcal{B}_0$ by a permanent deformation induced by growth. Since the elastic deformation $\boldsymbol{F}_e$ is measured from $\mathcal{B}_n(t)$, the intermediate state $\mathcal{B}_n(t)$ is also referred to as the *natural* configuration. The mapping from $\mathcal{B}_0$ to $\mathcal{B}_n(t)$, as mapped by growth tensor $\boldsymbol{F}_g$, can then be interpreted as the motion induced by free growth of the body without storage of any elastic energy. Hence, the natural state $\mathcal{B}_n(t)$ continuously evolves with time under $\boldsymbol{F}_g$. In rate form, the growth kinematics is characterized by the spatial velocity gradient $\boldsymbol{\ell} = \dot{\boldsymbol{F}}\boldsymbol{F}^{-1}$ ($\dot{\blacksquare}$ denoting the material time derivative of $\blacksquare$) which is additively decomposed into $\boldsymbol{\ell} = \boldsymbol{\ell}_e + \boldsymbol{\ell}_g$ (see Appendix Aa). Here, $\boldsymbol{\ell}_e = \dot{\boldsymbol{F}}_e \boldsymbol{F}_e^{-1}$ and $\boldsymbol{\ell}_g = \boldsymbol{F}_e \boldsymbol{L}_g \boldsymbol{F}_e^{-1}$ are, respectively, the elastic and growth-induced spatial velocity gradients. The tensor $\boldsymbol{L}_g = \dot{\boldsymbol{F}}_g \boldsymbol{F}_g^{-1}$ is interpreted as the velocity gradient in the natural configuration $\mathcal{B}_n(t)$.

An important concept in morphoelasticity is that of incompatibility which relates to growth-induced residual stresses (Skalak et al. 1996). The natural state $\mathcal{B}_n$, obtained via elastic unloading under $\boldsymbol{F}_e^{-1}$ (or equivalently via unconstrained growth under $\boldsymbol{F}_g$), may not be compatible from a continuum standpoint (see Fig. 1). This is due to the fact that the unloaded state (or equivalently the freely grown state) can only be defined *locally* and may not lead to a *global* stress-free configuration. Consequently, the tensors $\boldsymbol{F}_e$ and $\boldsymbol{F}_g$ cannot, in general, be mathematically written as gradients of a displacement field. In a nutshell, if $\boldsymbol{F}_g$ results in an incompatible deformation, the elastic part $\boldsymbol{F}_e$ acts to restore compatibility in the current (deformed) state $\mathcal{B}$. This leads to the development of growth-induced residual stresses (Garikipati 2009).

Constitutive relations. Based on finite inelasticity, the complete mechanical response of a growing body under externally applied loads and constraints can be decoupled into elastic and inelastic. The elastic response, which corresponds to the deformation from $\mathcal{B}_n$ to $\mathcal{B}$, is characterized by suitable constitutive relations while the growth-induced inelastic deformation is prescribed in terms of certain evolution laws. Considering the growing body as a hyperelastic solid, its elastic response involves introducing a strain-energy density $\psi_n(\boldsymbol{F}_e)$. Here, the subscript n denotes that the energy density is defined as stored energy per unit *natural* volume (Huang et al. 2021). Furthermore, if the elastic response is isotropic, $\psi_n(\boldsymbol{F}_e)$ should be expressed as an isotropic scalar function of the form:

$$\psi_n(\boldsymbol{F}_e) = \psi_n(\boldsymbol{b}_e) = \psi_n(I_1, I_2, I_3) \tag{3}$$

where $\boldsymbol{b}_e = \boldsymbol{F}_e \boldsymbol{F}_e^T$ is the elastic left Cauchy–Green deformation tensor and I_1, I_2, I_3 are the invariants of $\boldsymbol{b}_e$. In this special case of isotropy, the Cauchy stress tensor $\boldsymbol{\sigma}$ can be derived from $\psi_n(\boldsymbol{b}_e)$ using (see Appendix Ab):

$$\boldsymbol{\sigma} = \frac{2}{J_e}\frac{\partial \psi_n}{\partial \boldsymbol{b}_e}\boldsymbol{b}_e \tag{4}$$

Thus, capturing the elastic response of a growing isotropic solid requires the knowledge of spatial tensor $\boldsymbol{b}_e(\boldsymbol{x}, t)$ at all times t. This is achieved by solving the following evolution equation (see Appendix Ac):

$$\mathcal{L}(\boldsymbol{b}_e) = \dot{\boldsymbol{b}}_e - \boldsymbol{\ell}\boldsymbol{b}_e - \boldsymbol{b}_e\boldsymbol{\ell}^T = -\boldsymbol{d}_g \tag{5}$$

where $\mathcal{L}(\blacksquare)$ denotes the Lie derivative of a tensor field $\blacksquare$ and $\boldsymbol{d}_g$ is growth-induced inelastic flow rate. In continuum mechanics, the Lie derivative is a very useful quantity as it can be used to directly measure the rate of inelastic deformation in the solid (in this case $\boldsymbol{d}_g$). To understand this, consider the case when $\mathcal{L}(\boldsymbol{b}_e) = \boldsymbol{0}$, which consequently yields $\boldsymbol{b}_e = \boldsymbol{F}\boldsymbol{F}^T = \boldsymbol{b}$, where $\boldsymbol{b}$ is the left Cauchy–Green deformation tensor. This result implies that when $\mathcal{L}(\boldsymbol{b}_e)$ vanishes, the spatial tensor $\boldsymbol{b}_e$ convects with the flow under $\boldsymbol{\ell}$ and thus, the deformation is purely elastic. However, in case $\mathcal{L}(\boldsymbol{b}_e) \neq \boldsymbol{0}$, the deformation contains an inelastic part, expressed by the inelastic flow rate $\boldsymbol{d}_g$, which can be derived as $\boldsymbol{d}_g = \boldsymbol{\ell}_g\boldsymbol{b}_e + \boldsymbol{b}_e\boldsymbol{\ell}_g^T$ (see Appendix Ac), where $\boldsymbol{\ell}_g = \boldsymbol{F}_e\dot{\boldsymbol{F}}_g\boldsymbol{F}_g^{-1}\boldsymbol{F}_e^{-1}$. Therefore, to complete the model, we need to specify a *growth law* in terms of $\boldsymbol{F}_g(\boldsymbol{X}, t)$. For isotropic growth, $\boldsymbol{F}_g$ is an isotropic tensor of the form $\boldsymbol{F}_g = g\boldsymbol{I}$, where $g(\boldsymbol{X}, t)$ is called the growth ratio and $\boldsymbol{I}$ is the second-order identity matrix. Consequently, the flow rate $\boldsymbol{d}_g$ for isotropic growth becomes:

$$\boldsymbol{d}_g = 2\frac{\dot{g}}{g}\boldsymbol{b}_e \tag{6}$$

2.2 Why morpho-viscoelasticity?

The classical morphoelasticity theory discussed above assumes the growing body remains elastic over the growth timescale (Jones and Chapman 2012). This assumption limits the application of morphoelasticity theory to multicellular systems or aggregates that exhibit complex elasto-visco-plastic behavior (Preziosi et al. 2010). This behavior is attributed to mechanisms that can relax the stress at the time scale of growth. These mechanisms include cellular activities like adhesion bonds remodeling, cell neighbor exchange, and cell division. Thus, to effectively model aggregate growth, it is crucial to integrate these cell-scale activities as additional inelastic deformations into the morphoelasticity theory. While some attempts in this direction have been made in the past by phenomenologically reflecting dissipative mechanisms (Ambrosi and Preziosi 2009; Yan et al. 2021), a more detailed exploration into the individual role of cellular processes is warranted, given their significant influence on the mechanics of concentrated aggregates.

For instance, volumetric growth in dense cell aggregates, like spheroids, is primarily driven by a process called *proliferation* (Gillies and Cabernard 2011; Zhao et al. 2022), which involves two concurrent yet fundamentally distinct processes: (i) cell expansion denoting an increase in cell size and (ii) cell division denoting an increase in cell number. Given that proliferation drives growth, it becomes imperative to differentiate between expansion and division as they exhibit different mechanosensitivity and exert different effects on the growth dynamics. While cell expansion is a *non-dissipative* process, cell divisions can result in stress relaxation (Wyatt et al. 2015). Another cellular mechanism of importance is *intercalation* which involves an exchange of neighbors. A noteworthy study, relevant to our purpose, was conducted by Marmottant et al. (2009) in which the authors performed parallel plate compression experiments on non-proliferating aggregates. They observed that aggregates exhibited elastic, viscous, and plastic behaviors owing to intercalation.

For these reasons, we here develop a proliferation-based continuum theory for aggregate growth in which cells can simultaneously expand, divide, and intercalate. Since the developed theory accounts for the visco-hyperelastic response of the growing aggregate, we term it as *morpho-viscoelasticity*. Moreover, the theory follows a bottom-up methodology based on coarse-graining, resulting in a multiscale model. This entails the use of appropriate statistical quantities and internal state variables (ISVs) that facilitate the translation of microscopic cell-scale information to the macro-level. Such an approach offers three main advantages: (1.) establishing a clear correlation between continuum laws and underlying mechanisms, (2.) effective modeling of complex feedback and mechanosensitivity, and (3.) distinguishing between the effects of different cellular activities that might seem similar if considered in a phenomenological manner.

3 Morpho-viscoelasticity through the lens of the transient network theory

To implement the bottom-up approach for deriving our constitutive relations, we employ the theoretical framework of transient network theory (TNT) wherein each continuum point is imagined to consist of an underlying network of vectors (Vernerey et al. 2017). A complete description of macroscopic mechanical behavior at a point is then provided by the statistics of the network embedded within that point. We now discuss TNT in the context of confluent cell ensembles (Bandil and Vernerey 2023).

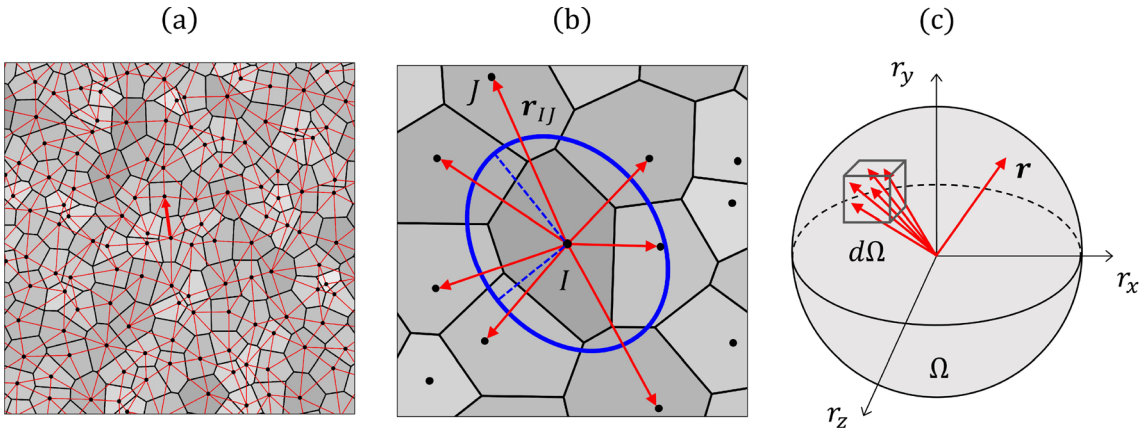

Fig. 2 **a** Cell monolayer as a 2D network of segment vectors. **b** Illustration of conformation tensor as an ellipse (in blue) for a cell I. **c** Conformation space $\Omega \in \mathbb{R}^3$

3.1 Network representation of aggregate

Consider a continuum point $\mathcal{P} \in \mathcal{B}(t)$ with spatial coordinate $\boldsymbol{x}$. Assuming that the continuum body is sufficiently large in comparison with the characteristic dimension of the constituent cell, the point $\mathcal{P}$, on a mesoscale, can be envisioned as an *aggregate* of a large number of cells (see Fig. 1). The same aggregate can be conceptualized as a *network* of *segment* vectors $\boldsymbol{r}$, where $\boldsymbol{r}$ signifies a *physical* connection between the geometric centers of two adjacent cells sharing a junction. In other words, $\boldsymbol{r}$ denotes a *topological* link between two neighboring cell sites (or nodes) and the aggregate can be viewed as a network of many such links (see Fig. 1). Now, in addition to being elastically deformed, the cells comprising the aggregate may also be simultaneously expanding, dividing, and intercalating. This behavior can alternatively be interpreted in terms of the network of segment vectors where the network *stores energy* while concurrently *remodeling*. The deformed state of the aggregate (engrained within point $\mathcal{P}$ at coordinate $\boldsymbol{x}$ and time t) can thus be determined from a corresponding deformation in the network. To establish this correspondence, let us first mathematically quantify the relationship between cells and segment vectors.

For ease of demonstration, we focus here on a two-dimensional (2D) network, although the formulation can be extended to three dimensions (3D). Consider a cell monolayer, represented as a 2D network of vectors $\boldsymbol{r}$, as shown in Fig. 2a. The geometry of any random cell I can be approximated from the conformation tensor $\boldsymbol{M}_I$, defined by (Graner et al. (2008)):

$$\boldsymbol{M}_I := \frac{1}{n_I} \sum_{J=1}^{n_I} \boldsymbol{r}_{IJ} \otimes \boldsymbol{r}_{IJ} \tag{7}$$

where n_I is the number of neighbors of cell I, $\boldsymbol{r}_{IJ}$ is the segment vector between cell I and its neighbor J, and $\otimes$ denotes the dyadic product. The shape of cell I is then estimated by the eigenvalues and eigendirections of the conformation tensor $\boldsymbol{M}_I$, represented by a confidence ellipse (ellipsoid in 3D), as shown in Fig. 2b. More precisely, the dimensions of the semi-major axes and the principal directions of the ellipse (ellipsoid in 3D) are, respectively, given by the square roots of the eigenvalues and the eigendirections of the associated conformation tensor. For example, the volume V_I of the confidence ellipsoid for a cell I (in 3D) can be calculated from $\boldsymbol{M}_I$ as $V_I = (4\pi/3)\sqrt{\det \boldsymbol{M}}$.

The above illustration shows how the network of segment vectors and the aggregate of cells can be considered as 'mathematical duals' of each other. We are now interested in bridging the gap between the fine scales (individual segments) and the coarse scales (network level). To do this, we make use of the mean-field approximation, by which the network deformation is approximated as the averaged deformation of its constituent vectors. For the deformed network state to be representative of the macroscopic deformation at coordinate $\boldsymbol{x}$ and time t, this averaging must be *statistically homogeneous*. This means that the continuum description provided by the network should be independent of network size. In the TNT, the network size is measured by the total number, say $n(\boldsymbol{x}, t)$, of vectors comprising the network. To satisfy statistical homogeneity, the network should be large enough so that the averaged result becomes independent of $n(\boldsymbol{x}, t)$. Therefore, one can imagine the network (or correspondingly the aggregate) to be composed of a large number $n(\boldsymbol{x}, t)$ of vectors (or correspondingly $N(\boldsymbol{x}, t)$ of cells) at any instant. Given this, the segment vector $\boldsymbol{r} = (r_x, r_y, r_z)$ can be treated as a continuous random variable that assumes all possible conformations, i.e., $r_x, r_y, r_z \in (-\infty, \infty)$, in a *conformation space* $\Omega \in \mathbb{R}^3$. Here, Ω can be understood as some *virtual* or theoretical space, with basis $\{r_x, r_y, r_z\}$, in which

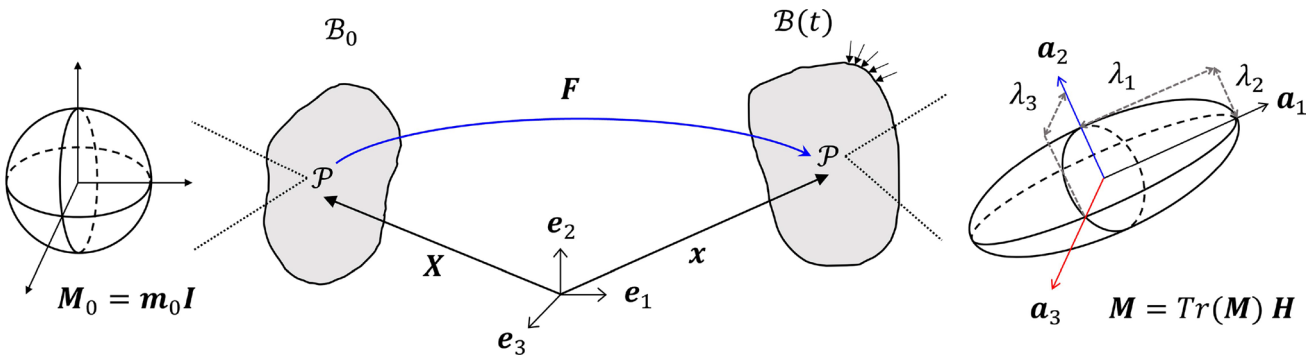

Fig. 3 Geometric illustration of mean conformation tensor $\boldsymbol{M}$ in the initial and current frames. The eigenvalues $(\lambda_1^2, \lambda_2^2, \lambda_3^2)$ of $\boldsymbol{M}$ can be expressed in terms of shape parameters $\gamma_1, \gamma_2, \gamma_3$ as $\lambda_1^2 = \mathrm{Tr}\,(\boldsymbol{M})\gamma_1$, $\lambda_2^2 = \mathrm{Tr}\,(\boldsymbol{M})\gamma_2$, and $\lambda_3^2 = \mathrm{Tr}\,(\boldsymbol{M})\gamma_3$

each coordinate denotes a segment vector $\boldsymbol{r}$, as shown in Fig. 2c.

3.2 Mean conformation tensor (texture tensor)

An averaged depiction of the network can now be indicated by a mean conformation tensor, $\boldsymbol{M}(\boldsymbol{x}, t)$, defined as the mean of $\boldsymbol{r} \otimes \boldsymbol{r}$ over space Ω, i.e.,

$$\boldsymbol{M}(\boldsymbol{x}, t) := \int_{\Omega} p(\boldsymbol{x}, \boldsymbol{r}, t)\, \boldsymbol{r} \otimes \boldsymbol{r}\, d\Omega \tag{8}$$

where $p(\boldsymbol{x}, \boldsymbol{r}, t)$ is a probability density function (*pdf*) that measures the likelihood of a segment vector to exist in conformation $\boldsymbol{r} \in \Omega$. The mean conformation tensor, also commonly known as *texture tensor* (Aubouy et al. 2003; Ishihara et al. 2017; Graner et al. 2008), represents the averaged geometry of cells in the aggregate in the form of a *mean cell*. That is the tensor $\boldsymbol{M}(\boldsymbol{x}, t)$ describes the averaged deformed *shape* and *size* of the cells comprising the aggregate. Note that the texture tensor $\boldsymbol{M}$ is statistically homogeneous, and thus, allows us to connect micro- and macro-level descriptions. To show how $\boldsymbol{M}$ geometrically represents the macroscopic deformed state at a continuum point, we employ another well-known macroscopic quantity called structure tensor, denoted by $\boldsymbol{H}(\boldsymbol{x}, t)$ (Kao et al. 2011). Let $\boldsymbol{a}_1, \boldsymbol{a}_2, \boldsymbol{a}_3$ be the eigendirections[1] of $\boldsymbol{M}$. The texture tensor $\boldsymbol{M}$ can now be split as $\boldsymbol{M} = \mathrm{Tr}\,(\boldsymbol{M})\boldsymbol{H}$, where the structure tensor $\boldsymbol{H}$ is given by:

$$\boldsymbol{H} = \gamma_1 \boldsymbol{a}_1 \otimes \boldsymbol{a}_1 + \gamma_2 \boldsymbol{a}_2 \otimes \boldsymbol{a}_2 + \gamma_3 \boldsymbol{a}_3 \otimes \boldsymbol{a}_3 \tag{9}$$

Here $\gamma_1, \gamma_2, \gamma_3$ are the eigenvalues of $\boldsymbol{H}$ and denote shape parameters that control the shape anisotropy of $\boldsymbol{M}$. The shape parameters verify the conditions $0 < \gamma_1, \gamma_2, \gamma_3 < 1$ and $\gamma_1 + \gamma_2 + \gamma_3 = 1$. These conditions on shape parameters ensure that $\mathrm{Tr}\,(\boldsymbol{H}) = 1$ and the eigenvalues of $\boldsymbol{H}$ are positive. The structure tensor $\boldsymbol{H}$ thus provides a measure of the deformed shape of the mean cell (see Fig. 3). When $\gamma_1 = \gamma_2 = \gamma_3 = 1/3$, the tensor $\boldsymbol{H}$ reduces to $\boldsymbol{H} = (1/3)\boldsymbol{I}$ which denotes an isotropic (or spherical) mean cell.

The next task is to understand how the texture tensor $\boldsymbol{M}$ carries the notion of *deformation* under $\boldsymbol{F}$ (or $\boldsymbol{\ell}$). Before that, it is important to explore the nature of the body's *response* under deformation. For this, we look at the *pdf* $p_0(\boldsymbol{X}, \boldsymbol{r}_0) = p(\boldsymbol{X}, \boldsymbol{r}_0, 0)$ of segment vectors in their initial (undeformed) conformations $\boldsymbol{r}_0$ in state $\mathcal{B}_0$ where $\boldsymbol{x} = \boldsymbol{X}$. Following the TNT, the isotropic response of an elastic solid implies that the distribution given by the *pdf* p_0 is such that it results in an isotropic texture tensor $\boldsymbol{M}_0(\boldsymbol{X})$ of the form:

$$\boldsymbol{M}_0(\boldsymbol{X}) = \int_{\Omega} p_0(\boldsymbol{X}, \boldsymbol{r}_0)\, \boldsymbol{r}_0 \otimes \boldsymbol{r}_0\, d\Omega = m_0(\boldsymbol{X})\boldsymbol{I} \tag{10}$$

where $\boldsymbol{M}_0(\boldsymbol{X}) = \boldsymbol{M}(\boldsymbol{X}, 0)$ is the texture tensor in $\mathcal{B}_0$ and m_0 is statistically related to the lengths, r_0, of segment vectors in their initial (undeformed) conformations $\boldsymbol{r}_0$ (see Appendix Ad for details). In this study, we limit ourselves to isotropic solids (see Fig. 3). The initial (undeformed) volume $V_0(\boldsymbol{X})$ of the mean cell thus becomes $V_0 = (4\pi/3)\sqrt{\det \boldsymbol{M}_0} = (4\pi/3)m_0^{3/2}$. Consequently, the initial (undeformed) volume $\mathcal{V}_0(\boldsymbol{X})$ of the continuum point at $\boldsymbol{X}$ can be calculated as $\mathcal{V}_0 = N_0 V_0$, where $N_0(\boldsymbol{X}) = N(\boldsymbol{X}, 0)$ is the initial number of cells in the aggregate. Note that in continuum mechanics, the impression of continuum 'point' (or 'particle') refers to a part of the body with some volume as opposed to some point mass (Holzapfel 2000). We now move ahead to characterize *deformation* in terms of the texture tensor $\boldsymbol{M}(\boldsymbol{x}, t)$.

3.3 Evolution of the texture tensor

Consider a network with $n(\boldsymbol{x}, t)$ vectors in the deformed state $\mathcal{B}(t)$ at any time t. As the continuum point $\mathcal{P}$, located

[1] For an isotropic solid, the eigendirections $(\boldsymbol{a}_1, \boldsymbol{a}_2, \boldsymbol{a}_3)$ would be the principal directions of elastic stretch in the spatial frame. This will become clear in sec. 3.5 on elastic deformation.

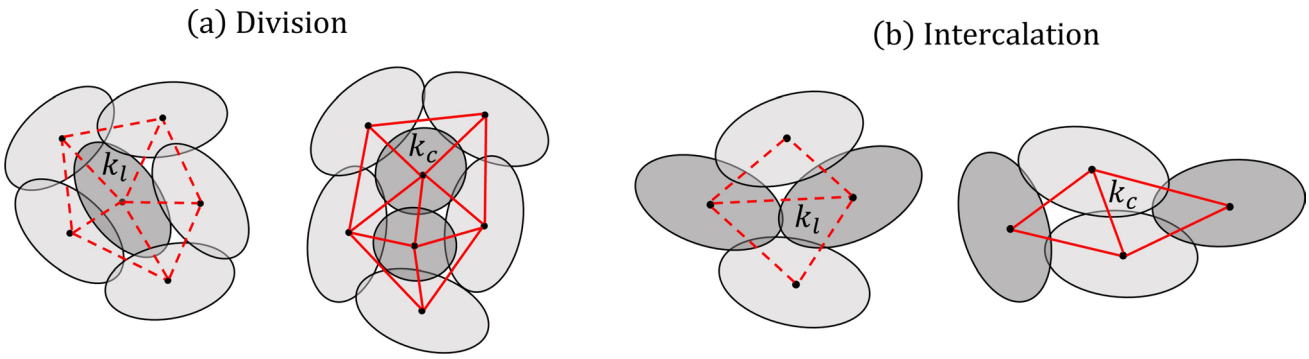

Fig. 4 Illustration of cell rearrangements resulting in creation and loss of segment vectors during **a** division and **b** intercalation

at position $\boldsymbol{x}$, deforms under spatial velocity gradient $\boldsymbol{\ell}(\boldsymbol{x},t)$, the underlying segment vectors are assumed to deform affinely under $\boldsymbol{\ell}$ as $\dot{\boldsymbol{r}} = \boldsymbol{\ell}\boldsymbol{r}$. This *affine* assumption entails that the macroscopic tensor fields—deformation gradient $\boldsymbol{F}$ (and consequently $\boldsymbol{\ell}$)—are translated uniformly throughout the conformation space Ω. In other words, $\boldsymbol{F}$ (and consequently $\boldsymbol{\ell}$) are independent of conformation $\boldsymbol{r}$. In addition to segment vectors changing their conformations with rate $\boldsymbol{\ell}$, some new segment vectors can be created while some existing segment vectors can be lost from the network. This situation arises when cells *rearrange* under division (see Fig. 4a) and/or intercalation (see Fig. 4b). All of these events contribute to modifying the current *pdf* $p(\boldsymbol{x},\boldsymbol{r},t)$, which is shown in Appendix Ae to follow the given evolution equation, known as the Fokker–Planck equation:

$$\dot{p} = -\boldsymbol{\ell} : \left(\frac{\partial}{\partial \boldsymbol{r}} \otimes (p\boldsymbol{r})\right) - k_c\left(1 - \frac{1}{f}\right)p_c - k_l p - \frac{\dot{f}}{f}p \quad (11)$$

Here $(:)$ denotes the double dot product and $f(\boldsymbol{x},t) = n(\boldsymbol{x},t)/n_t$ is the fraction of the current number of segment vectors in the network. $n_t > n$ is an arbitrary constant that denotes the maximum number of segment vectors that can be present in the network. Each term in Eq. (11) can be now understood as follows. The first term models change in *pdf* p owing to affine kinematics. The second term accounts for the creation (or appearance) of new segment vectors with a kinetic rate $k_c(\boldsymbol{x},t)$. The newly created segment vectors follow a distribution given by *pdf* $p_c(\boldsymbol{x},\boldsymbol{r},t)$. The third term models the loss (or disappearance) of existing segment vectors with a kinetic rate $k_l(\boldsymbol{x},\boldsymbol{r},t)$. The last term represents the change in *pdf* p due to an effective change in the number of segment vectors owing to creation and loss events.

Note. In general, the loss rate k_l can be a function of current conformation $\boldsymbol{r}$. This situation could arise when cells have a 'preferred direction' for rearrangement. For example, during convergent extension, cells intercalate preferentially along the dorsal–ventral (DV) axis (Keller et al. 2000) to achieve tissue elongation. In this case, k_l would be different for conformations oriented along the DV axis than the conformations aligned perpendicular to it. In this situation, the response of the solid would be direction-dependent, resulting in anisotropic behavior. This is beyond the scope of the current study.

Owing to isotropy restriction, $k_l = k_l(\boldsymbol{x},t)$ here becomes independent of $\boldsymbol{r}$, consequently yielding (see Appendix Ae):

$$\frac{\dot{f}}{f} = k_c\left(\frac{1}{f} - 1\right) - k_l \quad (12)$$

Since the texture tensor $\boldsymbol{M}$ directly depends on the *pdf* p (via Eq. (8)), we can obtain, using the Fokker–Planck Eq. (11), the expression for Lie derivative $\mathcal{L}(\boldsymbol{M})$, as:

$$\mathcal{L}(\boldsymbol{M}) = \dot{\boldsymbol{M}} - \boldsymbol{\ell}\boldsymbol{M} - \boldsymbol{M}\boldsymbol{\ell}^T = -k_c\left(1 - \frac{1}{f}\right)\boldsymbol{M}_c - k_l\boldsymbol{M} - \frac{\dot{f}}{f}\boldsymbol{M} \quad (13)$$

where $\boldsymbol{M}_c = \int_\Omega p_c\, \boldsymbol{r}\otimes\boldsymbol{r}\, d\Omega$ is the mean conformation tensor corresponding to newly created vectors. The tensor $\boldsymbol{M}_c$ can thus be used, to denote the mean cell configuration that would be attained as a result of cell rearrangement. It can be seen from Eqs. (12) and (13) that $\mathcal{L}(\boldsymbol{M})$ models the rate of inelastic deformation owing to cell rearrangements, which are characterized by rates k_c and k_l. Now recall the discussion from sec. 2.1 regarding the significance of Lie derivative in representing inelastic deformation. We see, from Eqs. (12) and (13), that in the absence of rearrangements, i.e., when $k_c = k_l = 0$, $\mathcal{L}(\boldsymbol{M})$ vanishes, implying that $\mathcal{L}(\boldsymbol{M})$ measures the rate of inelastic deformation owing to cell rearrangements. However, $\mathcal{L}(\boldsymbol{M})$ may not characterize the total inelastic deformation in the aggregate, as explained in the following sections.

3.4 Inelastic deformation

As mentioned previously, cellular processes-induced inelastic (irreversible and time-dependent) deformation can be interpreted in terms of network *remodeling*. We show here that remodeling can be the result of two types of events, which we denote here as extrinsic and intrinsic remodeling. Extrinsic remodeling occurs at the level of a group of segment vectors changing their connectivity. In contrast, intrinsic remodeling manifests as an evolution of individual segment vectors' inherent properties. We now discuss each of the modes of remodeling with the help of suitable examples.

Note—For clarity of notation, we will omit the arguments $\boldsymbol{x}$ and t here on and only use them *ad hoc*. Furthermore, any statistical quantity and ISV introduced henceforth will generally depend on $\boldsymbol{x}$ and t unless otherwise specified.

3.4.1 Extrinsic remodeling

Extrinsic remodeling refers to changes in the network connectivity or *topology*. Modifying the network topology requires breaking some of the existing connections (or links) and forming new ones. Recognizing that these actions mean the same as the loss and creation of segment vectors, cell rearrangements-induced inelastic deformation can be deemed as extrinsic remodeling. Since cell rearrangements alter network topology (see Fig. 4), they are also called *topological transitions*. Mathematically, extrinsic remodeling (or topological transitions) is thus represented by changes in the *pdf* p owing to rates k_c, k_l, and $\dot{f}/f$ in the Fokker–Planck Eq. (11). Consequently, the Lie derivative $\mathcal{L}(\boldsymbol{M})$ (Eq. (13)) of the texture tensor can now be interpreted as the rate of inelastic deformation due to extrinsic remodeling events (or topological transitions). Let us now explore extrinsic remodeling with the help of the example of cell intercalation.

Intercalation. Intercalation, also commonly called T1 transitions, is a process that involves an exchange or swapping of neighbors without altering the cell count N. That is, intercalation results in a change in network topology without affecting the number n of segment vectors, as shown in Fig. 4b. At this point, we invoke the relationship between n and N, given by $n = zN$, where z measures the averaged number of neighbors or links per cell and is assumed to be constant. Hence change in cell count directly relates to the change in the number of segment vectors, measured by rate $\dot{f}/f = \dot{n}/n = \dot{N}/N$. Now for T1 transitions, we have $\dot{N}/N = \dot{f}/f = 0$, which gives (from Eq. (12)):

$$k_c\left(\frac{1}{f} - 1\right) = k_l \tag{14}$$

Substituting the above relation into Eq. (13), we obtain the rate of inelastic deformation due to T1 transitions, given by $\mathcal{L}(\boldsymbol{M})$ as:

$$\mathcal{L}(\boldsymbol{M}) = -k_T(\boldsymbol{M} - \boldsymbol{M}_T) \tag{15}$$

where $k_T(= k_l)$ is the rate of T1 transitions and is simply given by the kinetic rate k_l of loss of segment vectors. The tensor $\boldsymbol{M}_T(= \boldsymbol{M}_c)$ is the extrinsically remodeled mean cell configuration as a result of intercalation.

3.4.2 Intrinsic remodeling

As opposed to extrinsic remodeling, intrinsic remodeling does not alter the topology of the network. That is, the Lie derivative $\mathcal{L}(\boldsymbol{M})$ remains unaffected by this kind of remodeling (from Eq. (13)). Instead, intrinsic remodeling transforms the intrinsic (or inherent) attributes of the individual segment vectors themselves. A key cellular process that triggers intrinsic remodeling is that of cell expansion as discussed below.

Expansion. In discrete simulations (Barton et al. 2017), the process of cell expansion is modeled as an increase in the *preferred* (or natural) volume of the cells. Following this, cell expansion can be modeled as an increase in the *natural* volume, denoted by $V_n(\boldsymbol{x}, t)$, of the mean cell. The origin of natural volume V_n can be understood as follows. Consider a *fictitious* network in which all the constituent segment vectors, at any time, are in their natural (or relaxed) conformations, denoted by $\boldsymbol{r}_n$. Let the distribution of natural conformations in this fictitious network be given by some *pdf* $p_n(\boldsymbol{x}, \boldsymbol{r}_n, t)$. Consequently, we can define a fictitious texture tensor, $\boldsymbol{M}_n(\boldsymbol{x}, t)$, given by:

$$\boldsymbol{M}_n(\boldsymbol{x}, t) = \int_\Omega p_n(\boldsymbol{x}, \boldsymbol{r}_n, t)\, \boldsymbol{r}_n \otimes \boldsymbol{r}_n \, d\Omega \tag{16}$$

where the tensor $\boldsymbol{M}_n$ represents the *natural* mean cell. The cell expansion process can now be understood as segment vectors changing or *remodeling* their natural conformations, which in turn alters the *pdf* p_n, leading to the evolution of the natural mean cell configuration $\boldsymbol{M}_n$ (see Fig. 5). The material time derivative of $\boldsymbol{M}_n$, then, represents the rate of inelastic deformation owing to intrinsic remodeling. The notion of the evolution of a *natural* mean cell under expansion is similar to the evolution of natural (stress-free) state $\mathcal{B}_n$ under $\boldsymbol{F}_g$ in morphoelasticity. Therefore, the natural mean cell can also be recognized as the state of the mean cell that would be attained under unconstrained expansion. This further denotes that the *initial* natural mean cell coincides with the initial (undeformed) mean cell given by $\boldsymbol{M}_0$. Therefore, we obtain the initial conditions on $\boldsymbol{M}_n$ and p_n as $\boldsymbol{M}_n(0) = \boldsymbol{M}_0$ and $p_n(0) = p_0$.

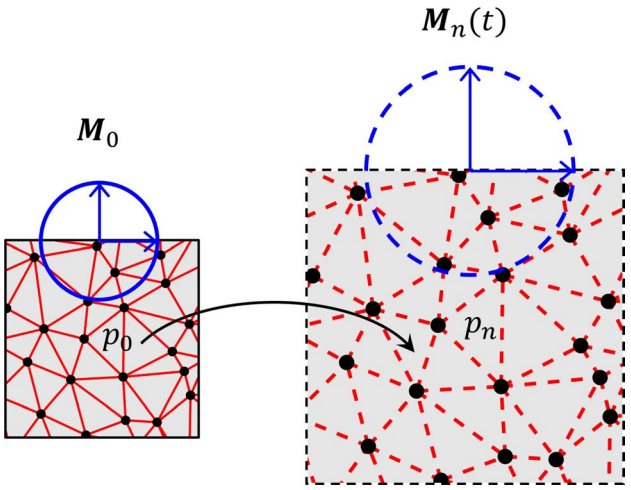

Fig. 5 Illustration of a fictitious network (denoted by red dashed links) and associated mean cell $\boldsymbol{M}_n$ undergoing intrinsic remodeling under isotropic cell expansion

From the above initial conditions, we see that the initial shape of the natural mean cell is described by $\boldsymbol{M}_0$, which, in this study, is spherical owing to solid isotropy. Furthermore, suppose the response of the isotropic solid under intrinsic remodeling remains isotropic. In that case, the natural mean cell preserves its spherical geometry and only evolves via a change in its volume $V_n = (4\pi/3)\sqrt{\det \boldsymbol{M}_n}$. Under these circumstances, the natural mean cell configuration can be represented by an isotropic form of the tensor $\boldsymbol{M}_n = m_n \boldsymbol{I}$, where m_n is an ISV that is statistically related to the natural conformation lengths r_n, akin to m_0. From $\boldsymbol{M}_n(0) = \boldsymbol{M}_0$, we obtain the initial condition $m_n(0) = m_0$ on ISV m_n. In the present work, we only focus on isotropic responses, i.e., the rate of inelastic deformation owing to intrinsic remodeling can be measured in terms of scalar quantity, $\dot{m}_n$. Figure 5 shows that in the case of isotropy, the fictitious network is simply a *photographic enlargement* of the initial (undeformed) state. This also entails the fact that no topological rearrangements occur in the evolving fictitious network.

Finally, we can complete the cell expansion model by prescribing an evolution equation for m_n, or more precisely $V_n = (4\pi/3)m_n^{3/2}$. For convenience, we introduce a normalized measure for V_n, denoted by ζ_i and defined as:

$$\zeta_i := \frac{V_n}{V_0} = \left(\frac{m_n}{m_0}\right)^{3/2} \tag{17}$$

where recall that V_0 characterizes the mean cell volume in $\mathcal{B}_0$. From Eq. (17), ζ_i is an ISV that measures permanent volumetric deformation owing to the inelastic process of cell expansion, hence termed as *inelastic expansion ratio*. An evolution law for the increase in V_n can now be prescribed in terms of ζ_i which, in this study, is assumed to follow a simple exponential kinetics with expansion rate k_E as (Barton et al. (2017)):

$$\dot{\zeta}_i = k_E \zeta_i \tag{18}$$

3.4.3 Combined extrinsic and intrinsic remodeling

Unlike T1 transition which only contributes to extrinsic remodeling and cell expansion which only contributes to intrinsic remodeling, the process of **cell division** contributes to both modes of remodeling. In other words, it not only modifies the Lie derivative $\mathcal{L}(\boldsymbol{M})$ via topological changes (see Fig. 4a) but also alters the natural mean cell configuration $\boldsymbol{M}_n$. Let us first deduce the rate $\mathcal{L}(\boldsymbol{M})$ of topological transition-induced inelastic deformation due to division followed by the effect of division on the natural mean cell, as characterized by $\dot{V}_n$ (or $\dot{\zeta}_i$). The process of cell division has classically been modeled, similar to expansion, with exponential kinetics as (Montel et al. (2012)):

$$\dot{\eta} = k_D \eta \tag{19}$$

where $\eta = N/N_0$ is the *cell number ratio* and k_D is the associated division rate. Here, recall that N_0 is the initial number of cells at a material point in $\mathcal{B}_0$. Akin to T1 transitions, the division rate k_D is also given by the loss rate k_l. In terms of the ratio $\dot{f}/f$, we write $\dot{f}/f = \dot{N}/N = \dot{\eta}/\eta = k_D = k_l$, which when substituted in Eq. (12), gives:

$$\frac{k_c}{2}\left(\frac{1}{f} - 1\right) = k_D \tag{20}$$

Further substituting the above into Eq. (13), we obtain the Lie derivative owing to division as:

$$\mathcal{L}(\boldsymbol{M}) = -2k_D\left(\boldsymbol{M} - \boldsymbol{M}_D\right) \tag{21}$$

where the tensor $\boldsymbol{M}_D (= \boldsymbol{M}_c)$, analogous to $\boldsymbol{M}_T$, is the extrinsically remodeled mean cell configuration due to division. From Eqs. (15) and (21), we observe that the inelastic deformation induced by topological changes under cell division is similar to that of T1 transitions. However, differences in behavior may arise due to variations in the mechanosensitivities of the rates k_D and k_T, as discussed later in sec. 4.

To understand the role of cell divisions in intrinsic remodeling, we again resort to the division algorithm implemented in discrete cell-based models (Barton et al. 2017). According to this, as the volume $V = (4\pi/3)\sqrt{\det \boldsymbol{M}}$ of the mean cell exceeds a certain threshold V^*, where V^* is a constant, it splits into two daughter cells, each with volume $V/2$. According to this, cell division is an isochoric inelastic process that induces no permanent volume change. In finite inelasticity theories like morphoelasticity, the permanent volume change is measured in terms of volume ratio J_i (J_g

in morphoelasticity), defined as the ratio of natural volume to initial (undeformed) volume at a continuum point. For our system, we can calculate J_i as:

$$J_i = \frac{\mathscr{V}_n}{\mathscr{V}_0} = \frac{NV_n}{N_0 V_0} = \eta\zeta_i \tag{22}$$

where $\mathscr{V}_n = NV_n$ is the macroscopic natural volume. Further assuming no cell expansion (i.e., $k_E = 0$), enforcing the condition $\dot{J}_i = 0$ and using Eqs. (19) and (22), we get:

$$\dot{J}_i = \dot{\eta}\zeta_i + \eta\dot{\zeta}_i = 0 \implies \frac{\dot{\zeta}_i}{\zeta_i} = -\frac{\dot{\eta}}{\eta} \implies \dot{\zeta}_i = -k_D\zeta_i \tag{23}$$

This simple relation indicates that cell division, in addition to increasing the cell count η, also reduces the natural mean cell volume V_n (equivalently m_n). Although expansion and division occur simultaneously during proliferation, they are independently regulated processes. In other words, division can occur without expansion, and expansion can occur without division (Ateshian et al. 2012). Consequently, the mechanics of proliferation can be modeled by superimposing deformations induced by both these inelastic processes. Hence, we combine Eqs. (18) and (23) to obtain the governing equation for proliferation in terms of ζ_i as:

$$\dot{\zeta}_i = (k_E - k_D)\zeta_i \tag{24}$$

which shows that division competes with the kinetics of expansion during proliferation. Equation (24) thus represents intrinsic remodeling owing to proliferation.

Following ζ_i, we introduce a dimensionless measure for mean cell volume V, given by ISV $\zeta = V/V_0$ and termed as *cell size ratio*. The division criterion is then fulfilled when the cell size ratio ζ exceeds a certain threshold $\zeta^* = V^*/V_0$. The volume ratio $J = \det \boldsymbol{F}$ can then be expressed in terms of ISVs η and ζ as:

$$J = \frac{\mathscr{V}}{\mathscr{V}_0} = \frac{NV}{N_0 V_0} = \eta\zeta \tag{25}$$

where $\mathscr{V} = NV$ is the macroscopic total volume. Note that this expression for J explicitly separates the total volume change into—a change in cell count η and a change in cell size ζ, thus accounting for proliferation-driven growth. Further identifying $J_e = V/V_n$ as the elastic volumetric deformation, we can write $\zeta = J_e\zeta_i$ and $J = J_eJ_i = J_e\eta\zeta_i$, where recall that $J_i = \eta\zeta_i$ is the inelastic (or permanent) volumetric deformation.

3.5 Elastic deformation

Classical morphoelasticity theory (Ambrosi and Mollica 2002) focuses solely on intrinsic remodeling due to volumetric growth (or cell expansion), while coarse-grained models (Ishihara et al. 2017; Graner et al. 2008) consider only extrinsic remodeling from topological transitions. This is evident from the corresponding Lie derivatives: $\mathcal{L}(\boldsymbol{b}_e)$ (Eq. (5)), which does not account for extrinsic remodeling events, and $\mathcal{L}(\boldsymbol{M})$ (Eq. (13)), which does not capture intrinsic remodeling. Thus, to measure elastic deformation in proliferating aggregates, we require a quantity that encompasses both—extrinsic remodeling (i.e., $\mathcal{L}(\boldsymbol{M})$) and intrinsic remodeling (i.e., the evolution of the natural mean cell configuration $\boldsymbol{M}_n$). To address this, we introduce the *normalized texture tensor*, denoted by $\boldsymbol{\mu}$, defined as:

$$\boldsymbol{\mu} := \frac{1}{m_n}\boldsymbol{M} \tag{26}$$

The tensor $\boldsymbol{\mu}$, then, provides an accurate measure of elastic deformation in the network, as discussed below. It is first important to mention that Eq. (26) assumes an isotropic response of the solid, characterized by tensors $\boldsymbol{M}_0 = m_0\boldsymbol{I}$ and $\boldsymbol{M}_n = m_n\boldsymbol{I}$. If the solid's response is anisotropic, these tensors will, in general, no longer remain isotropic, and consequently, the Eq. (26) will need to be modified to account for anisotropy. To now illustrate that the normalized texture tensor $\boldsymbol{\mu}$ is a true descriptor of elastic deformation, it would be sufficient to show that its Lie derivative $\mathcal{L}(\boldsymbol{\mu})$ provides a complete depiction of inelastic deformation in the network. The Lie derivative $\mathcal{L}(\boldsymbol{\mu})$, as derived using Eqs. (13), (17), and (26), is expressed as:

$$\mathcal{L}(\boldsymbol{\mu}) = \dot{\boldsymbol{\mu}} - \boldsymbol{\ell}\boldsymbol{\mu} - \boldsymbol{\mu}\boldsymbol{\ell}^T = \frac{1}{m_n}\mathcal{L}(\boldsymbol{M}) - \frac{2}{3}\frac{\dot{\zeta}_i}{\zeta_i}\boldsymbol{\mu} \tag{27}$$

From the above equation, we see that the normalized texture tensor $\boldsymbol{\mu}$ evolves under extrinsic as well as intrinsic remodeling. The current morpho-viscoelasticity theory (as given by $\mathcal{L}(\boldsymbol{\mu})$) thus effectively couples growth mechanics with viscous dissipation. In contrast to existing elastic-visco-growth theories (Ambrosi and Preziosi 2009), we here do not explicitly decompose the inelastic part (i.e., $\boldsymbol{F}_e^{-1}\boldsymbol{F}$) into viscous and growth deformations. Instead, we here (implicitly) categorize total inelastic deformation into extrinsic and intrinsic remodeling owing to different cellular processes. This approach of interpreting cellular processes-induced inelastic deformations in terms of network remodeling not only allows us to bridge the cell and tissue scale behavior but also comprehensively model the individual effects of the involved cellular processes (see Table 1).

Let us now consider the case when $\mathcal{L}(\boldsymbol{\mu})$ vanishes, i.e., no network remodeling occurs. In this situation, the normalized texture tensor becomes $\boldsymbol{\mu} = \boldsymbol{F}\boldsymbol{\mu}_0\boldsymbol{F}^T$, where $\boldsymbol{\mu}_0 = \boldsymbol{\mu}(0)$ can be evaluated as $\boldsymbol{\mu}_0 = \boldsymbol{M}(0)/m_n(0) = \boldsymbol{M}_0/m_0 = \boldsymbol{I}$. From this result, we get $\boldsymbol{\mu} = \boldsymbol{F}\boldsymbol{F}^T = \boldsymbol{b}$, which shows that the normalized texture tensor $\boldsymbol{\mu}$ reduces to the classical $\boldsymbol{b}$ tensor. In the general case, when $\mathcal{L}(\boldsymbol{\mu}) \neq \boldsymbol{0}$, the tensor $\boldsymbol{\mu}$

Table 1 Comparison among various continuum models for tissues and cell aggregates

Continuum model	Cell-level description	Extrinsic remodeling		Intrinsic remodeling	
		Intercalation	Division	Expansion	Division
Morphoelasticity (Rodriguez et al. 1994; Ambrosi and Mollica 2002)				✓	
Elasto-visco-growth (Ambrosi and Preziosi 2009; Yan et al. 2021)		✓	✓	✓	
Coarse-grained (Ishihara et al. 2017; Graner et al. 2008	✓	✓			
TNT (current model)	✓	✓	✓	✓	✓

thus bears resemblance to tensor $\boldsymbol{b}_e$ and consequently is directly related to $\boldsymbol{F}_e$. However, in contrast to morphoelasticity and other elasto-visco-plastic theories (Preziosi et al. 2010) where $\boldsymbol{b}_e = \boldsymbol{F}_e\boldsymbol{F}_e^T$, we here do not mathematically express $\boldsymbol{\mu}$ in terms of $\boldsymbol{F}_e$. Nevertheless, it is still interesting to show that $\boldsymbol{\mu}$ is indeed related to $\boldsymbol{F}_e$. For this, we take the determinant of relation (26) and obtain, $\det \boldsymbol{\mu} = (\det \boldsymbol{M})/m_n^3 = (V/V_n)^2 = J_e^2 = (\det \boldsymbol{F}_e)^2$, and thus,

$$J_e = \sqrt{\det \boldsymbol{\mu}} \tag{28}$$

Moreover, when the mean cell is in its natural state, i.e., $\boldsymbol{M} = \boldsymbol{M}_n = m_n\boldsymbol{I}$, we obtain $\boldsymbol{\mu} = \boldsymbol{I}$, signifying no elastic deformation or equivalently $\boldsymbol{F}_e = \boldsymbol{I}$. Again note that the fact $\boldsymbol{\mu} = \boldsymbol{I}$ in the natural state is a consequence of isotropy. The key takeaway is that, for an isotropic solid, the macroscopic elastic deformation can be fully computed from the normalized texture tensor $\boldsymbol{\mu}$. Consequently, the material constitutive relations for energy density ψ_n (Eq. (3)) and Cauchy stress tensor $\boldsymbol{\sigma}$ (Eq. (4)) can be formulated in terms of $\boldsymbol{\mu}$ as:

$$\psi_n(\boldsymbol{\mu}) = \psi(I_1, I_2, I_3) \quad \text{and} \quad \boldsymbol{\sigma} = \frac{2}{J_e}\frac{\partial \psi_n}{\partial \boldsymbol{\mu}}\boldsymbol{\mu} \tag{29}$$

where I_1, I_2, I_3 are now the invariants of tensor $\boldsymbol{\mu}$.

4 Model illustration

In this section, we demonstrate the use of the TNT-based morpho-viscoelasticity theory. The key element of the current model is that Eq. 5 in morphoelasticity can now be generalized using morpho-viscoelasticity to:

$$\mathcal{L}(\boldsymbol{\mu}) = \dot{\boldsymbol{\mu}} - \boldsymbol{\ell}\boldsymbol{\mu} - \boldsymbol{\mu}\boldsymbol{\ell}^T = -\boldsymbol{d}_E - \boldsymbol{d}_T - \boldsymbol{d}_D \tag{30}$$

where $\boldsymbol{d}_E, \boldsymbol{d}_T$ and $\boldsymbol{d}_D$ are, respectively, the inelastic flow rates due to expansion, T1 transition, and division. The above equation considers the fact that expansion, T1 transition, and division are independent processes, each exerting its effect on aggregate mechanics. Let us now derive explicit expressions for $\boldsymbol{d}_E, \boldsymbol{d}_T$ and $\boldsymbol{d}_D$ from the Lie derivative $\mathcal{L}(\boldsymbol{\mu})$ (Eq. (27)).

For illustrative purposes, we will be examining an example problem solved using the classical morphoelasticity theory by Ambrosi and Mollica (2002). Investigating the same example problem using the morpho-viscoelasticity theory allows us to not only illustrate the current model but also make direct comparisons with the existing morphoelasticity theory. For these reasons, we employ the same hyperelastic material model for ψ_n as used by Ambrosi and Mollica (2002), which is the Blatz-Ko hyperelasticity material model given by:

$$\psi_n = \frac{G}{2}\left[(I_1 - 3) - \frac{2}{q}(J_e^q - 1)\right] \tag{31}$$

where $I_1 = \mathrm{Tr}(\boldsymbol{\mu})$, $J_e = \sqrt{\det \boldsymbol{\mu}}$, G and q are material parameters related to the linear elasticity constants: Young's modulus E and Poisson's ratio ν, through the relationships $G = E/(2(1+\nu))$ and $q = -2\nu/(1-2\nu)$. Note that the strain-energy density provided by Eq. (31) accommodates elastic compressibility and material isotropy. The Cauchy stress tensor $\boldsymbol{\sigma}$ can then be derived from Eq. (29), resulting in:

$$\boldsymbol{\sigma} = \frac{G}{J_e}\left[-(J_e)^q\boldsymbol{I} + \boldsymbol{\mu}\right] \tag{32}$$

Notice that the stress-free ($\boldsymbol{\sigma} = \boldsymbol{0}$) configuration is represented by $\boldsymbol{\mu} = \boldsymbol{I}$ which is also the initial condition on $\boldsymbol{\mu}$.

4.1 Expansion

We have already seen that expansion does not involve any topological changes (or extrinsic remodeling) and only contributes to $\mathcal{L}(\boldsymbol{\mu})$ through the evolution of ζ_i. Substituting Eq. (18) into Eq. (27) yields the associated flow rate $\boldsymbol{d}_E$ as:

$$\boldsymbol{d}_E = \frac{2}{3}k_E\boldsymbol{\mu} \tag{33}$$

The crucial point is that cell expansion is the sole inelastic mechanism that effectively leads to permanent volume change. Other inelastic mechanisms like division and

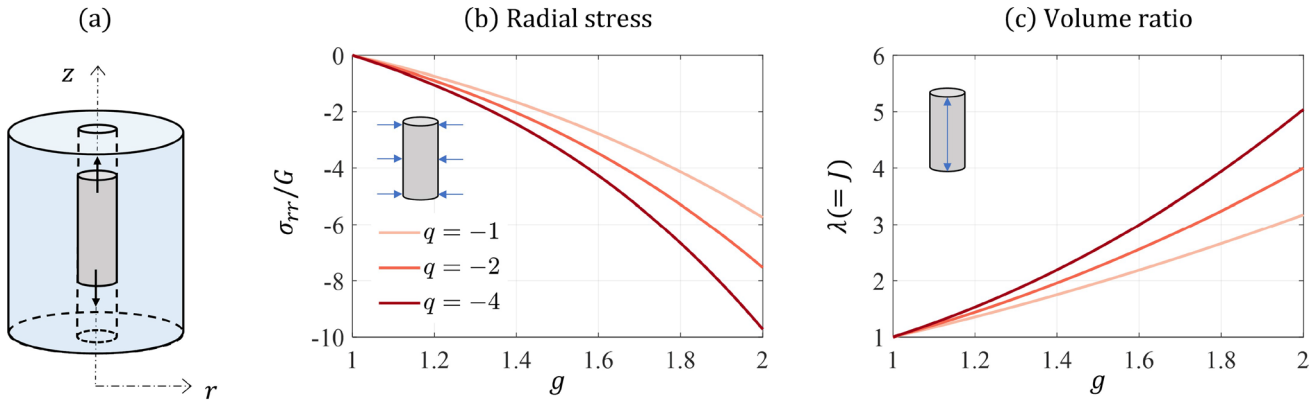

Fig. 6 **a** Schematic of spheroid growing inside a rigid cylinder. **b** Normalized radial wall stress σ_{rr}/G. **c** Spheroid volume ratio $J = \det \boldsymbol{F}$ (same as stretch ratio λ in this example)

intercalation do not induce any permanent volume alterations at the macroscale. Therefore, since the morphoelasticity theory only accounts for inelastic volumetric deformation, the expansion model in the current theory must degenerate to morphoelasticity theory in case of isotropic growth. That is $\boldsymbol{d}_E$ and $\boldsymbol{d}_g$ must be equivalent in case $\boldsymbol{\ell}_g = \dot{g}/g\boldsymbol{I}$, which gives:

$$\frac{\dot{g}}{g} = \frac{k_E}{3} \tag{34}$$

The above relationship illustrates that isotropic cell expansion leads to isotropic volumetric growth, given by $\boldsymbol{\ell}_g = (k_E/3)\boldsymbol{I}$. The only distinction between the expansion model in the current theory and classical morphoelasticity lies in characterizing the driving force for active deformation in terms of an expansion law for k_E rather than a growth law for $\boldsymbol{\ell}_g$.

We now demonstrate the above idea by solving a simple problem of **homogeneous deformation** of a multicellular spheroid. This example serves to understand how the TNT model aligns with morphoelasticity theory in the absence of topological rearrangements (i.e., when $k_D, k_T = 0$ and resultantly $\boldsymbol{d}_D, \boldsymbol{d}_T = \boldsymbol{0}$). In this case, the governing equation (30) for the evolution of elastic deformation tensor $\boldsymbol{\mu}$, using Eq. (33), becomes:

$$\dot{\boldsymbol{\mu}} = \boldsymbol{\ell}\boldsymbol{\mu} + \boldsymbol{\mu}\boldsymbol{\ell}^T - \frac{2}{3}k_E\boldsymbol{\mu} \tag{35}$$

The example problem we look at involves a cylindrical spheroid grown inside a rigid cylinder as shown in Fig. 6a. Since the spheroid is unable to deform radially (and circumferentially), the kinematics is described by deformation gradient $\boldsymbol{F}$ (and equivalently by velocity gradient $\boldsymbol{\ell}$) of the form:

$$\boldsymbol{F} = \text{Diag}\{1,\ 1,\ \lambda\} \implies \boldsymbol{\ell} = \text{Diag}\left\{0,\ 0,\ \frac{\dot{\lambda}}{\lambda}\right\} \tag{36}$$

where λ is the stretch ratio along the vessel or z axis. Moreover, we assume that the driving force for deformation is provided by active cell expansion occurring at a constant rate $k_E = k_E^0$. Substituting $k_E = k_E^0$ in Eq. (34) and applying the initial condition $g(t = 0) = 1$, results in an isotropic and homogeneous form of volumetric growth law represented as:

$$g(t) = \exp\left(\frac{k_E^0}{3}t\right) \tag{37}$$

The stretch ratio λ can be found by first numerically integrating the Eq. (35) using the forward Euler scheme. Once we determine $\boldsymbol{\mu}(t)$, we then impose the traction-free boundary condition on the z surfaces of the spheroid to obtain $\lambda(t)$. Given the homogeneity of the deformation fields, the boundary condition simplifies to $\sigma_{zz} = 0$, where σ_{zz} represents the z component of the Cauchy stress tensor $\boldsymbol{\sigma} = \text{Diag}\{\sigma_{rr}, \sigma_{rr}, \sigma_{zz}\}$, with σ_{rr} being the radial (and hoop) stress component. The resulting plots for radial stress σ_{rr} (Fig. 6b) and stretch ratio λ (Fig. 6c) as functions of g are consistent with the analytical solutions derived by Ambrosi and Mollica (2002) using morphoelasticity. Hence, the key takeaway from this illustration is that the morpho-viscoelasticity theory converges to morphoelasticity theory for isotropic growth in the absence of any rearrangements (i.e., when $k_D, k_T = 0$).

4.2 T1 transition

As T1 transitions result only in extrinsic remodeling, the $\dot{\zeta}_i/\zeta_i$ term in Eq. (27) vanishes and we get, by substituting Eq. (15) into Eq. (27), the inelastic flow rate $\boldsymbol{d}_T$ as:

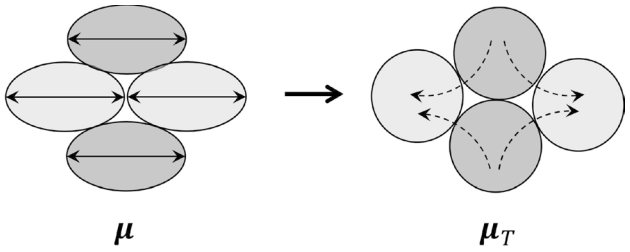

Fig. 7 Biased T1 transitions

$$\boldsymbol{d}_T = k_T(\boldsymbol{\mu} - \boldsymbol{\mu}_T) \tag{38}$$

where $\boldsymbol{\mu}_T = \boldsymbol{M}_T/m_n$, akin to $\boldsymbol{M}_T$, represents the preferred state the cells aim to attain via intercalating, and thus informs about the *flow* resulting from T1 transitions. Unlike cell expansion which is an isotropic process, topological transitions, in general, exhibit directionality.[2] Hence, effective mathematical modeling of the topological transitions requires including the directional bias. For example, cells in a stretched monolayer dissipate stresses by adopting a less elongated (or distorted) geometry through intercalation, as shown in Fig. 7(Ishihara et al. 2017; Bandil and Vernerey 2023). This behavior can be modeled by prescribing an isotropic form to the tensor $\boldsymbol{\mu}_T$, i.e., $\boldsymbol{\mu}_T = \mu_T \boldsymbol{I}$, where μ_T is yet unknown. To find the unknown μ_T, we make use of the fact that T1 transitions do not induce any permanent volume change (as can be seen from Eq. (22)). From this, we can obtain the tensor $\boldsymbol{\mu}_T$ (see Appendix Af) as:

$$\boldsymbol{\mu}_T = \frac{3}{\mathrm{Tr}\,(\boldsymbol{\mu}^{-1})}\boldsymbol{I} \tag{39}$$

which when substituted into Eq. (38) yields the T1 transition-induced flow rate $\boldsymbol{d}_T$ as:

$$\boldsymbol{d}_T = k_T\left(\boldsymbol{\mu} - \frac{3}{\mathrm{Tr}\,(\boldsymbol{\mu}^{-1})}\boldsymbol{I}\right) \tag{40}$$

We show in Appendix Ag, how the inelastic flow rate $\boldsymbol{d}_T$ in Eq. (40) satisfies dissipation inequality and hence is thermodynamically admissible. Notice from Eq. (40) that in case the elastic deformation in cells is isotropic (i.e., the tensor $\boldsymbol{\mu}$ is isotropic), then the flow rate $\boldsymbol{d}_T$ vanishes, meaning that intercalation does not induce any effective deformation at the macroscale in this scenario.

Another important feature of T1 transitions is that cells can only intercalate if they are distorted beyond a certain threshold (Marmottant et al. 2009). To account for this *yield* behavior, we first need a measure of elastic distortion in the cells. For this, we introduce another ISV, denoted by χ, and defined as:

$$\chi := \sqrt{\frac{3}{2}\boldsymbol{\mu}' : \boldsymbol{\mu}'} \tag{41}$$

where $\boldsymbol{\mu}'$ denotes the deviatoric (traceless) part of $\boldsymbol{\mu}$ given by:

$$\boldsymbol{\mu}' = \frac{\boldsymbol{\mu}}{I_1} - \frac{1}{3}\boldsymbol{I} = \boldsymbol{H} - \frac{1}{3}\boldsymbol{I} \tag{42}$$

Recognize that the expression for χ in Eq. (41) is analogous to the von Mises stress used in J_2 flow plasticity theory with the deviatoric part of $\boldsymbol{\mu}$ used instead of Cauchy stress $\boldsymbol{\sigma}$. Further using Eq. (9) and considering that principal directions $\boldsymbol{a}_1, \boldsymbol{a}_2, \boldsymbol{a}_3$ align with the coordinate system's axes, we can rewrite χ in terms of shape parameters $\gamma_1, \gamma_2, \gamma_3$ as:

$$\chi = \sqrt{\frac{3}{2}\left[\left(\gamma_1 - \frac{1}{3}\right)^2 + \left(\gamma_2 - \frac{1}{3}\right)^2 + \left(\gamma_3 - \frac{1}{3}\right)^2\right]} \geq 0 \tag{43}$$

It can be seen from the above expression that there is no distortion (i.e., $\chi = 0$) only if $\gamma_1 = \gamma_2 = \gamma_3 = 1/3$ (in which case $\boldsymbol{\mu}' = \boldsymbol{0}$). Any deviation of χ from 0, thus, indicates the extent of elastic distortion in cell shape. Notably, like I_1, χ is also an invariant of $\boldsymbol{\mu}$. As the driving force for the process of T1 transition comes from elastic distortion χ, the yield phenomena can be modeled in terms of the kinetic rate k_T as:

$$k_T = k_T(\chi) \text{ if } \chi > \chi^* \tag{44}$$

and $k_T = 0$, otherwise. This definition for the kinetic rate k_T ensures that cells can only intercalate (i.e., $\boldsymbol{d}_T \neq \boldsymbol{0}$) if they are distorted beyond a threshold χ^*. Thus allowing us to capture the complex elasto-visco-plastic behavior in terms of a scalar ISV k_T. Different functional forms for $k_T(\chi)$ can be proposed depending on the nature of T1 transitions. To further simplify the model, we assume that $k_T = k_T^0$, if $\chi > \chi^*$, and $k_T = 0$, otherwise. This straightforward expression allows us to qualitatively model the influence of T1 transitions on the mechanics of a growing aggregate, which is the primary objective of this study.

4.2.1 Effect of T1 transition on constrained spheroid growth

To show the effect of T1 transition on growth mechanics, we study the same problem of the homogeneous growth of the constrained cylindrical spheroid (see schematic of Fig. 8), as studied in the previous sec. 4.1. In this example, we consider that cells can only expand (with the rate $k_E = k_E^0$) and intercalate without dividing (i.e., $k_D = 0$). The governing Eq. (35) for $\dot{\boldsymbol{\mu}}$ for this case becomes, using Eq. (40):

[2] This directionality has nothing to do with the change in material orientation and effectively its response to deformation.

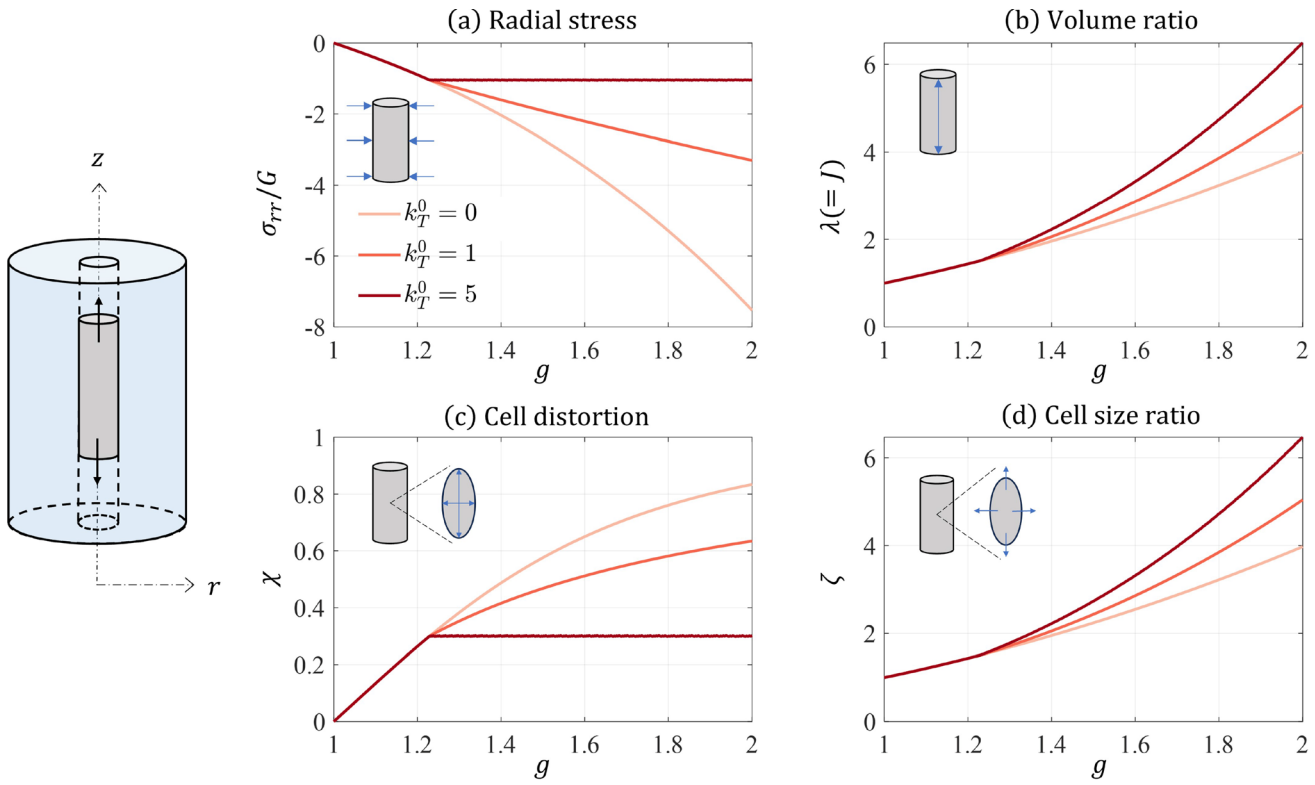

Fig. 8 Effect of biased T1 transition on: **a** normalized radial wall stress σ_{rr}/G, **b** spheroid volume ratio J (same as stretch ratio λ in this example), **c** cell shape distortion χ, and **d** cell size ratio ζ, as plotted against growth ratio g. Simulation parameters: $\chi^* = 0.3$ and $q = -2$

$$\dot{\boldsymbol{\mu}} = \boldsymbol{\ell}\boldsymbol{\mu} + \boldsymbol{\mu}\boldsymbol{\ell}^T - \frac{2}{3}k_E^0\boldsymbol{\mu} - k_T\left(\boldsymbol{\mu} - \frac{3}{\mathrm{Tr}\,(\boldsymbol{\mu}^{-1})}\boldsymbol{I}\right) \tag{45}$$

Following the same solution procedure mentioned earlier, we plot the results in Fig. 8 for different values of T1 transition rate k_T^0, where $k_T^0 = 0$ denotes the results of morphoelasticity. We observe that as soon as cells start intercalating (i.e., when χ exceeds χ^*), distortion χ (Fig. 8c) decreases with increase in k_T^0. Notably, χ approaches a homeostatic value (equal to χ^*) for higher values of k_T^0. The reduction in cell distortion χ is associated with the directional bias of T1 transitions. When the mean cell shape is elastically distorted (beyond yield), cells intercalate, resulting in a more spherical mean cell geometry and thus reduced χ. T1 transitions have been observed to relieve stresses in passive tissues and aggregates (Ishihara et al. 2017; Marmottant et al. 2009). Figure 8a illustrates how cells dissipate wall stress σ_{rr} through intercalation in a growing aggregate. Relaxation of compressive stress σ_{rr} is accompanied by an increase in elastic volumetric deformation J_e (which is < 1 due to compression). This consequently increases cell size $\zeta = J_e\zeta_i$ (Fig. 8d) and the spheroid volume $J = J_eJ_i$ (Fig. 8b). Since $\eta = 1$ owing to $k_D^0 = 0$, we can write for this example:

$$\frac{\dot{\zeta}}{\zeta} = \frac{\dot{J}_e}{J_e} + k_E^0 \quad \text{and} \quad \frac{\dot{J}}{J} = \frac{\dot{J}_e}{J_e} + k_E^0 \tag{46}$$

As $\dot{J}_e/J_e > 0$ due to relaxation under T1 transitions, we see that T1 transitions promote both cell size ζ and volumetric growth J. Overall we observe that T1 transitions can influence cell shape (χ) and size (ζ) within a growing aggregate by relaxing stresses. The degree of relaxation is contingent upon the intercalation rate k_T^0, with higher rates leading to greater relaxation and isotropicity. Moreover, we also showed how the elasto-visco-plastic behavior of cell aggregates can be modeled by simply considering $k_T(\chi)$.

4.3 Division and proliferation

As division contributes to both extrinsic as well as intrinsic remodeling, the inelastic flow rate $\boldsymbol{d}_D$ can be derived using Eqs. (21) and (23) as (see Appendix Ah):

$$\boldsymbol{d}_D = k_D\left(\frac{4}{3}\boldsymbol{\mu} - 2\boldsymbol{\mu}_D\right) \tag{47}$$

where the tensor $\boldsymbol{\mu}_D = \boldsymbol{M}_D/m_n$ models the favored or the desired state that cells aim to attain, on average, by undergoing division. The topological changes induced by division also exhibit directionality, akin to T1 transitions. In the case

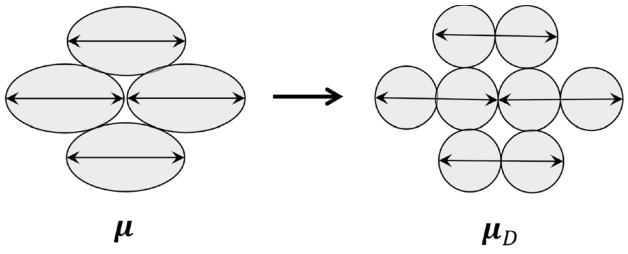

Fig. 9 Biased division

of division, directionality comes from the axis or orientation of cell division. Studies (Wyatt et al. 2015; Xu et al. 2016) show that cells in a stretched monolayer preferentially divide along their long axis instead of randomly chosen axes. In this way, they can dissipate more energy while preserving homeostasis and isotropic packing. This 'long axis' rule can be implemented using the tensor $\boldsymbol{\mu}_D$ which drives the flow under division (Bandil and Vernerey 2023). We first make use of the fact that biased divisions result in isotropic distributions as cells endeavor to achieve spherical geometries (see Fig. 9). This behavior is similar to that of T1 transitions and hence translates to $\boldsymbol{\mu}_D$ being an isotropic tensor. Combined with the inelastic incompressibility (or isochoric) constraint condition on division, we obtain (see Appendix Ah):

$$\boldsymbol{\mu}_D = \frac{2}{\mathrm{Tr}\,(\boldsymbol{\mu}^{-1})}\boldsymbol{I} \tag{48}$$

Substituting $\boldsymbol{\mu}_D$ from Eq. (48) in Eq. (47) yields the resultant macroscopic inelastic flow due to biased or oriented cell division as:

$$\boldsymbol{d}_D = k_D\left(\frac{4}{3}\boldsymbol{\mu} - \frac{4}{\mathrm{Tr}\,(\boldsymbol{\mu}^{-1})}\boldsymbol{I}\right) \tag{49}$$

Appendix Ai shows how the above flow rate for division is thermodynamically admissible. From Eq. (49), if the current deformed state of the aggregate is unbiased (i.e., $\boldsymbol{\mu}$ is isotropic), then division does not induce any inelastic flow (i.e., $\boldsymbol{d}_D = \boldsymbol{0}$). In this case, the sole impact of division is in increasing the cell count η and decreasing natural volume ζ_i. However, when cells are elastically distorted (i.e., $\chi > 0$) and exhibit unique principal directions, biased cell divisions affect the stress state of the system as we will see further.

Note on k_D: According to Xu et al. (2016), the larger the cell size−higher the probability of division. This implies that rate $k_D = k_D(\zeta)$, where the dependency has been proposed as an exponential form (Xu et al. (2016)):

$$k_D = k_D^0\left(1 - \exp\left(-\varrho_D\left[\zeta - \zeta^*\right]\right)\right) \quad \text{if} \quad \zeta > \zeta^* \tag{50}$$

and $k_D = 0$, otherwise. Here k_D^0 sets the upper limit on division rate, $\zeta^* = V^*/V_0$ is the threshold size ratio modeling aggregate plasticity due to division (Xu et al. 2015), and ϱ_D is a sensitivity parameter.

Apart from controlling the aggregate's stress state (Xu et al. 2016), cell division also plays an important role in maintaining the homeostatic state of cell packing (Farhadifar et al. 2007; Wyatt et al. 2015). To illustrate these concepts, we now explore the influence of division on spheroid growth mechanics by considering two cases: (1.) free growth and (2.) constrained growth.

4.3.1 Effect of division on free spheroid growth

Here, we demonstrate how homeostasis can be modeled using Eq. (24) through a simple example. Consider a freely proliferating aggregate under a constant expansion rate $k_E = k_E^0$. Owing to homogeneous expansion, no elastic energy is being stored during the process. In such a situation, since elastic volumetric deformation $J_e = 1$, we have $\zeta = \zeta_i$ and hence the cell size ratio ζ follows the same evolution equation (24) as ζ_i. From Fig. 10a, we see that with time, a steady state is reached and the mean cell size attains homeostasis (i.e., $\dot{\zeta} = k_E^0 - k_D = 0$). We can find out this steady-state value, say ζ^{ss}, by simply equating k_D in Eq. (50) to k_E^0, resulting in:

$$\zeta^{ss} = \zeta^* - \frac{1}{\varrho_D}\ln\left(1 - \frac{k_E^0}{k_D^0}\right) \tag{51}$$

The above solution reveals that homeostasis can only be achieved if the maximum division rate k_D^0 is more than the expansion rate k_E^0. If $k_E^0 > k_D^0$, then $\dot{\zeta} > 0$ always, resulting in a continuous increase in mean cell size throughout the growth process (see Fig. 10a). In this case, division rate $k_D < k_E^0$ (see Fig. 10b) and expansion dominate proliferation. This provides us with valuable insights into the relative rates of expansion and division within a growing population. With the aid of ISVs $(k_E, k_D, \zeta_i, \eta, \zeta)$, we can now also distinguish between the growth modes. To comprehend this, we employ the relationship in Eq. (25) which implies that:

$$\frac{\dot{J}}{J} = \frac{\dot{\eta}}{\eta} + \frac{\dot{\zeta}}{\zeta} \tag{52}$$

During the transient phase ($\dot{\zeta} \neq 0$), volumetric growth includes both an increase in cell size ζ and an increase in cell number η. However, when homeostasis is attained under suitable conditions, volumetric growth becomes entirely driven by the increase in cell number.

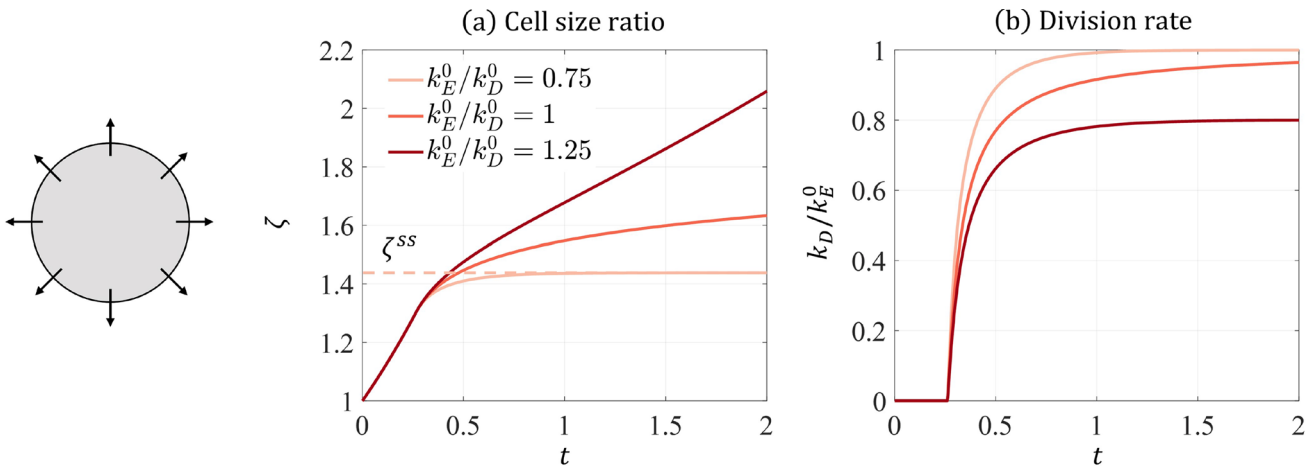

Fig. 10 **a** Cell size ratio ζ and **b** normalized division rate k_D/k_E^0, as plotted against time t for different values of rate k_D^0. Unit of t is $[1/k_E^0]$. Simulation parameters: $\zeta^* = 1.3$ and $\varrho_D = 10$

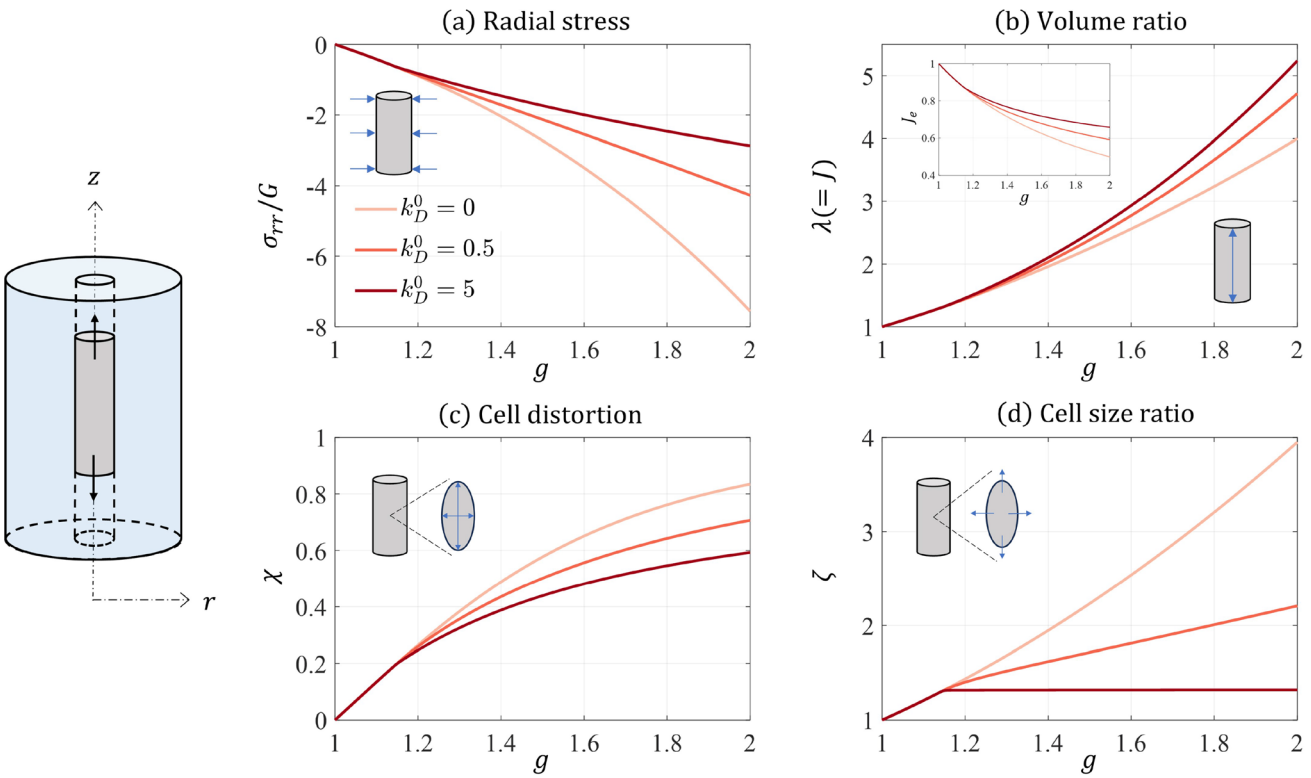

Fig. 11 Effect of biased division on: **a** normalized radial wall stress σ_{rr}/G, **b** spheroid volume ratio J (same as stretch ratio λ in this example), **c** cell shape distortion χ, and **d** cell size ratio ζ, as plotted against growth ratio g. Simulation parameters: $\zeta^* = 1.3$, $q = -2$, and $\varrho_D = 10$

4.3.2 Effect of division on constrained spheroid growth

Let us now solve the same example problem of constrained growth (see the schematic of Fig. 11) as introduced in sec. 4.1. The difference is that in addition to expanding, cells in the constrained spheroid can now also divide. In this case, since the cells are proliferating, the governing equation for ζ_i is given by Eq. (24) and the evolution Eq. (35) now becomes:

$$\dot{\boldsymbol{\mu}} = \boldsymbol{\ell}\boldsymbol{\mu} + \boldsymbol{\mu}\boldsymbol{\ell}^T - \frac{2}{3}k_E^0\boldsymbol{\mu} - k_D\left(\frac{4}{3}\boldsymbol{\mu} - \frac{4}{\mathrm{Tr}\,(\boldsymbol{\mu}^{-1})}\boldsymbol{I}\right) \tag{53}$$

As demonstrated in Fig. 11, once the cells start dividing (i.e., ζ exceeds ζ^*), distortion χ (Fig. 11c) and size ratio ζ (Fig. 11d), decrease with increase in k_D^0, with the effect on cell size ζ being significant. Again, since the mean cell shape is distorted under the confinement of the matrix, cell division results in a more ordered (or isotropic) packing, and thus reduced χ. Additionally, cell divisions have been observed to fluidize tissue by relieving stresses (Xu et al. 2016). This stress relaxation is evident in our results from Fig. 11a, which shows dissipation of wall stress σ_{rr} through division. One of the most notable effects of division is displayed in the mean cell size ratio ζ (Fig. 11d), wherein we observe that ζ eventually reaches a steady-state value for a high division rate of $k_D^0 = 5$. As shown in Fig. 11b, the model predicts that cell division promotes volumetric growth, leading to an overall increase in spheroid size with an increasing k_D^0. This response can be understood as follows. Substituting $\zeta = J_e\zeta_i$ in Eq. (52) and further using Eqs. (24) and (19), Eq. (52) can be rewritten as:

$$\frac{\dot{J}}{J} = \frac{\dot{J}_e}{J_e} + k_E \tag{54}$$

This simple relation shows that the overall volumetric deformation can be split into elastic volumetric deformation J_e and expansion (k_E) induced inelastic deformation. In this specific example problem, where $k_E = k_E^0$ is constant, the mechanism through which division influences the global spheroid size J is via relaxing compressive stress, thereby increasing J_e (see inset of Fig. 11b) and consequently leading to an increase in J.

Broadly speaking, the behavior of growing spheroid in response to division follows similar trends to those observed with intercalation (Fig. 8) in terms of stress relaxation (Figs. 8a and 11a) and promoting volumetric growth (Figs. 8b and 11b). However, the primary distinction lies in the fact that T1 transitions strongly regulates χ, while division significantly affects ζ. This disparity arises because shape distortion χ is the driving force for T1 transitions, whereas size ratio ζ drives division. As a result, T1 transitions help maintain cell shape (distortion) at its homeostatic value of χ^*, while division aids in maintaining cell size at its homeostatic value which depends on other factors including ζ^*. We notice from Figs. 8c,d and 11c,d that in the absence of any rearrangements (i.e., when $k_T^0, k_D^0 = 0$), cells undergo continuous distortion with growth, assuming highly deformed ellipsoidal shapes. Concurrently, cells exhibit volume expansion reaching large sizes. Both of these scenarios seem biologically improbable, as cells within spheroids are observed to maintain their shapes and sizes at moderate values, a state referred to as homeostasis (Tzur et al. 2009). This observation suggests that additional mechanisms (such as division and T1 transition) that regulate cell shape and size need to be taken into account while modeling the growth of spheroids.

5 Conclusion

To summarize, we here have presented a morpho-viscoelastic continuum theory to model growth in three-dimensional proliferating dense cell aggregates such as spheroids and organoids. Using the transient network theory, we have generalized the existing continuum mechanical models for confluent tissues in multiple ways: (1.) Additional inelastic mechanisms, namely division and intercalation, have been included. (2.) The model can now differentiate between different modes of growth (proliferation)—increase in cell size via expansion and increase in cell number via division. (3.) The model facilitates a thorough elucidation of the complex interplay between cell-level mechanics and aggregate-level growth. This involves the characterization of different cellular activities in terms of suitable ISVs and continuum field variables (4.) The model introduces a generalized measure of elastic deformation, given by normalized texture tensor, which incorporates all the cellular processes-induced inelastic mechanisms.

One of the most noteworthy contributions of the current study is to provide novel interpretations of inelastic deformations in an aggregate. We showed how inelastic deformation can be categorized into extrinsic and intrinsic network remodeling, where extrinsic remodeling deals with topological changes while intrinsic remodeling corresponds to changes in the properties of constituent network elements, in this case segment vectors. This categorization allowed us to comprehensively understand the influence of each of the cellular mechanisms—expansion, division, and intercalation—at the macroscale. For instance, we showed how division, which is one of the most prominent cellular morphogenetic processes, remodels the network extrinsically as well as intrinsically. Owing to this feature, we can now thoroughly model dissipation due to cell rearrangements alongside proliferation in aggregates under various loading and constraint conditions.

While the proposed model endeavors to make notable advancements in the mathematical modeling of growth, it is not without its limitations. One of the present formulation's major shortcomings is in characterizing anisotropic growth. Biological growth is not always isotropic. For instance, in cardiac and arterial tissues, the growth is characterized by an anisotropic form of the growth tensor (Ambrosi et al. 2011; Rodriguez et al. 1994). For such cases, the current formulation will need to be modified to

account for anisotropicity in the cell-level micro-structure driving growth. This will require redefining the material model for capturing anisotropic elastic response (Holzapfel et al. 2004). We recognize this as a promising prospect to further enhance the applicability of our framework. In this study, we solved simple example problems involving homogeneous deformation. To fully demonstrate the potential of the developed theory, it will be necessary to implement the model within the numerical framework of finite element analysis (FEA). This will enable us to study more intricate problems such as morphogenesis of tumor spheroids (Cheng et al. 2009; Kulwatno et al. 2021), tissue growth in polymeric scaffolds (Dhote and Vernerey 2014; Vernerey 2016), and mechanics of growth-induced residual stresses (Ambrosi and Mollica 2004).

Appendix

(a) Derivation of $\boldsymbol{\ell} = \boldsymbol{\ell}_e + \boldsymbol{\ell}_g$. Following the multiplicative decomposition $\boldsymbol{F} = \boldsymbol{F}_e\boldsymbol{F}_g$, the spatial velocity gradient $\boldsymbol{\ell} = \dot{\boldsymbol{F}}\boldsymbol{F}^{-1}$ can then be written as:

$$\begin{aligned}\boldsymbol{\ell} &= \left(\dot{\boldsymbol{F}}_e\boldsymbol{F}_g + \boldsymbol{F}_e\dot{\boldsymbol{F}}_g\right)\boldsymbol{F}_g^{-1}\boldsymbol{F}_e^{-1}\\ &= \dot{\boldsymbol{F}}_e\boldsymbol{F}_g\boldsymbol{F}_g^{-1}\boldsymbol{F}_e^{-1} + \boldsymbol{F}_e\dot{\boldsymbol{F}}_g\boldsymbol{F}_g^{-1}\boldsymbol{F}_e^{-1}\\ &= \dot{\boldsymbol{F}}_e\boldsymbol{F}_e^{-1} + \boldsymbol{F}_e\dot{\boldsymbol{F}}_g\boldsymbol{F}_g^{-1}\boldsymbol{F}_e^{-1}\end{aligned} \tag{55}$$

where the first term is called the elastic part of $\boldsymbol{\ell}$ and is denoted by $\boldsymbol{\ell}_e$, while the second term is the growth part denoted by $\boldsymbol{\ell}_g$. Therefore, we have:

$$\boldsymbol{\ell}_e = \dot{\boldsymbol{F}}_e\boldsymbol{F}_e^{-1} \quad \text{and} \quad \boldsymbol{\ell}_g = \boldsymbol{F}_e\dot{\boldsymbol{F}}_g\boldsymbol{F}_g^{-1}\boldsymbol{F}_e^{-1} \tag{56}$$

(b) Derivation of $\boldsymbol{\sigma}(\boldsymbol{b}_e)$. We start by employing the Clausius–Duhem inequality for an open system, expressed in the spatial frame as (Huang et al. 2021):

$$\mathscr{D} = \boldsymbol{\sigma} : \boldsymbol{\ell} - \rho\dot{\Psi} \geq 0 \tag{57}$$

where $\mathscr{D}$ is the mechanical dissipation rate, ρ is spatial mass density (defined as mass per unit current volume), and Ψ is the Helmholtz-free energy per unit mass. The strain-energy density ψ_n can be written in terms of Ψ as $\psi_n = \rho_n\Psi$, where $\rho_n = J_e\rho$ is called the natural mass density (defined as mass per unit natural volume). The term $\rho\dot{\Psi}$ can now be written as:

$$\rho\dot{\Psi} = \frac{1}{J_e}\dot{\psi}_n - \frac{1}{J_e}\frac{\dot{\rho}_n}{\rho_n}\psi_n \tag{58}$$

Substituting the above into Clausius–Duhem (Eq. (57)), we get:

$$\mathscr{D} = \boldsymbol{\sigma} : \boldsymbol{\ell} - \frac{1}{J_e}\dot{\psi}_n + \frac{1}{J_e}\frac{\dot{\rho}_n}{\rho_n}\psi_n \geq 0 \tag{59}$$

where the material time derivative $\dot{\psi}_n$ can be written (for isotropic material where $\psi_n = \psi_n(\boldsymbol{b}_e)$) as:

$$\dot{\psi}_n = \frac{d\psi_n}{dt} = \frac{\partial\psi_n}{\partial\boldsymbol{b}_e}:\dot{\boldsymbol{b}}_e = 2\frac{\partial\psi_n}{\partial\boldsymbol{b}_e}\boldsymbol{b}_e:\boldsymbol{\ell} + \frac{\partial\psi_n}{\partial\boldsymbol{b}_e}:\mathcal{L}(\boldsymbol{b}_e) \tag{60}$$

Using the above expression in Eq. (59), we get:

$$\mathscr{D} = \left(\boldsymbol{\sigma} - \frac{2}{J_e}\frac{\partial\psi_n}{\partial\boldsymbol{b}_e}\boldsymbol{b}_e\right):\boldsymbol{\ell} - \frac{1}{J_e}\frac{\partial\psi_n}{\partial\boldsymbol{b}_e}:\mathcal{L}(\boldsymbol{b}_e) + \frac{1}{J_e}\frac{\dot{\rho}_n}{\rho_n}\psi_n \geq 0 \tag{61}$$

For a hyperelastic material, the first term vanishes, resulting in:

$$\boldsymbol{\sigma} = \frac{2}{J_e}\frac{\partial\psi_n}{\partial\boldsymbol{b}_e}\boldsymbol{b}_e \tag{62}$$

(c) Derivation of $\mathcal{L}(\boldsymbol{b}_e)$. Starting with $\boldsymbol{b}_e = \boldsymbol{F}_e\boldsymbol{F}_e^T$, taking the material time derivative we get:

$$\dot{\boldsymbol{b}}_e = \dot{\boldsymbol{F}}_e\boldsymbol{F}_e^T + \boldsymbol{F}_e\dot{\boldsymbol{F}}_e^T \tag{63}$$

Substituting $\dot{\boldsymbol{F}}_e = \boldsymbol{\ell}_e\boldsymbol{F}_e$ (from Eq. (56)) in above, we get:

$$\begin{aligned}\dot{\boldsymbol{b}}_e &= \boldsymbol{\ell}_e\boldsymbol{F}_e\boldsymbol{F}_e^T + \boldsymbol{F}_e\boldsymbol{F}_e^T\boldsymbol{\ell}_e^T\\ &= \boldsymbol{\ell}_e\boldsymbol{b}_e + \boldsymbol{b}_e\boldsymbol{\ell}_e^T\end{aligned} \tag{64}$$

Further using $\boldsymbol{\ell}_e = \boldsymbol{\ell} - \boldsymbol{\ell}_g$, we obtain,

$$\dot{\boldsymbol{b}}_e = \boldsymbol{\ell}\boldsymbol{b}_e + \boldsymbol{b}_e\boldsymbol{\ell}^T - \left(\boldsymbol{\ell}_g\boldsymbol{b}_e + \boldsymbol{b}_e\boldsymbol{\ell}_g^T\right) \tag{65}$$

The Lie derivative of spatial tensor $\boldsymbol{b}_e$, defined by $\mathcal{L}(\boldsymbol{b}_e) := \dot{\boldsymbol{b}}_e - \boldsymbol{\ell}\boldsymbol{b}_e - \boldsymbol{b}_e\boldsymbol{\ell}^T$, can be expressed in terms of $\boldsymbol{\ell}_g$ using above expression as:

$$\mathcal{L}(\boldsymbol{b}_e) = -\left(\boldsymbol{\ell}_g\boldsymbol{b}_e + \boldsymbol{b}_e\boldsymbol{\ell}_g^T\right) = -\boldsymbol{d}_g \tag{66}$$

where $\boldsymbol{d}_g = \boldsymbol{\ell}_g\boldsymbol{b}_e + \boldsymbol{b}_e\boldsymbol{\ell}_g^T$ is the growth-induced inelastic flow rate. When $\boldsymbol{F}_g = g\boldsymbol{I}$, we get $\boldsymbol{\ell}_g = \boldsymbol{F}_e\boldsymbol{L}_g\boldsymbol{F}_e^{-1} = \dot{g}/g\boldsymbol{I}$, which yields $\boldsymbol{d}_g = 2\dot{g}/g\boldsymbol{b}_e$.

(d) Derivation of $\boldsymbol{M}_0$. Let $\boldsymbol{r}_0 = [r_{x0}, r_{y0}, r_{z0}]$ denote a random segment vector in the network embedded inside an arbitrary Lagrangian coordinate $\boldsymbol{X} \in \mathcal{B}_0$. The mean conformation tensor $\boldsymbol{M}_0$ is then given by:

$$\boldsymbol{M}_0 = \langle\boldsymbol{r}_0 \otimes \boldsymbol{r}_0\rangle = \begin{bmatrix}\langle r_{x0}^2\rangle & \langle r_{x0}r_{y0}\rangle & \langle r_{x0}r_{z0}\rangle\\ \langle r_{x0}r_{y0}\rangle & \langle r_{y0}^2\rangle & \langle r_{y0}r_{z0}\rangle\\ \langle r_{x0}r_{z0}\rangle & \langle r_{y0}r_{z0}\rangle & \langle r_{z0}^2\rangle\end{bmatrix} \tag{67}$$

where $\langle\blacksquare\rangle$ is the mean of $\blacksquare$ over conformation space Ω. For an isotropic distribution, we have $\langle r_{x0}r_{y0}\rangle = \langle r_{y0}r_{z0}\rangle = \langle r_{x0}r_{z0}\rangle = 0$ and $\langle r_{x0}^2\rangle = \langle r_{y0}^2\rangle = \langle r_{z0}^2\rangle$. Let r_0 be the length of segment

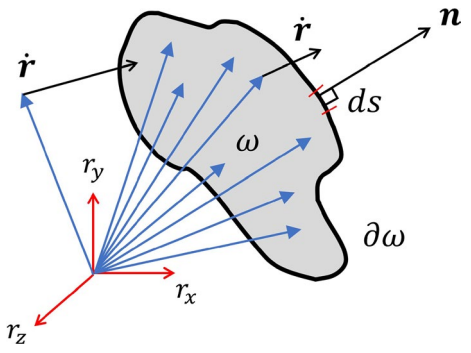

Fig. 12 Control volume ω in the conformation space Ω

vector $\boldsymbol{r}_0$. Hence $r_0^2 = r_{x0}^2 + r_{y0}^2 + r_{z0}^2$. Taking the mean, we get $\langle r_0^2\rangle = \langle r_{x0}^2\rangle + \langle r_{y0}^2\rangle + \langle r_{z0}^2\rangle$. From isotropy, we have $\langle r_{x0}^2\rangle = \langle r_{y0}^2\rangle = \langle r_{z0}^2\rangle = \langle r_0^2\rangle/3$. The tensor $\boldsymbol{M}_0$ in Eq. (67) thus becomes:

$$\boldsymbol{M}_0 = \frac{\langle r_0^2\rangle}{3}\begin{bmatrix}1&0&0\\0&1&0\\0&0&1\end{bmatrix} = \frac{\langle r_0^2\rangle}{3}\boldsymbol{I} = m_0\boldsymbol{I} \tag{68}$$

The scalar $m_0 = \langle r_0^2\rangle/3$ thus provides us with a measure of the average of the square of segment vector lengths in the network at initial equilibrium (i.e., $\mathcal{B}_0$). Similarly, the natural (or current equilibrium) configuration of the network, for an isotropic solid, is given by the tensor $\boldsymbol{M}_n = m_n\boldsymbol{I}$, where $m_n = \langle r_n^2\rangle/3$ measures the average of the square of the natural lengths r_n of the segment vectors.

(e) Evolution equation for the *pdf* p. We start by introducing a statistical quantity, $\phi(\boldsymbol{x},\boldsymbol{r},t) = f(\boldsymbol{x},t)p(\boldsymbol{x},\boldsymbol{r},t)$, which measures the fraction of segment vectors existing in conformation $\boldsymbol{r}$ per unit conformation space. The fraction f can be expressed in terms of ϕ as:

$$f(\boldsymbol{x},t) = \frac{n(\boldsymbol{x},t)}{n_t} = \int_\Omega \phi(\boldsymbol{x},\boldsymbol{r},t)\,d\Omega \tag{69}$$

Now consider an arbitrary fixed control volume $\omega \subset \Omega$ bounded by surface $\partial\omega$ as shown in Fig. 12. Let n_ω be the number of segment vectors inside ω at any time t. An evolution equation for ϕ (and consequently for the *pdf* p) can be derived by writing the conservation equation for $n_\omega = n_t\int_\omega \phi\,d\omega$ (Note that n_t is some constant). Now each point in conformation space Ω, denoted by vector $\boldsymbol{r}$, moves with velocity $\dot{\boldsymbol{r}} = \boldsymbol{\ell}\boldsymbol{r}$ (using the affine assumption). Net influx, say Q, of vectors through the surface $\partial\omega$ into the domain ω is then given by:

$$\begin{aligned} Q &= -\int_\omega \phi\dot{\boldsymbol{r}}\cdot\boldsymbol{n}\,ds \\ &= -\int_\omega \nabla\cdot(\phi\boldsymbol{\ell}\boldsymbol{r})\,d\omega \\ &\quad \text{(using divergence theorem)} \end{aligned} \tag{70}$$

where $\boldsymbol{n}$ is the normal to the elementary surface ds and the ∇ operator is defined in the basis $\{r_x, r_y, r_z\}$. Q here measures net change in the number of segment vectors inside the domain ω due to convection (or flow) under $\boldsymbol{\ell}$. Additionally, new segment vectors can be created or some existing segment vectors can be lost under (inelastic) rearrangement events. The conservation equation for n_ω can now written as:

$$\begin{aligned} \frac{\dot{n}_\omega}{n_t} &= \int_\omega \frac{d\phi}{dt}\,d\omega = -\int_\omega \nabla\cdot(\phi\boldsymbol{\ell}\boldsymbol{r})\,d\omega \\ &\quad + \int_\omega \xi_c\,d\omega - \int_\omega \xi_l\,d\omega \end{aligned} \tag{71}$$

where ξ_c and ξ_l are, respectively, the source (creation) and sink (loss) terms. Since the above conservation equation holds for any arbitrary domain $\omega \subset \Omega$, we can write from localization:

$$\begin{aligned} \frac{d\phi}{dt} &= -\nabla\cdot(\phi\boldsymbol{\ell}\boldsymbol{r}) + \xi_c - \xi_l \\ &= -\boldsymbol{\ell} : \nabla(\phi\boldsymbol{r}) + \xi_c - \xi_l \end{aligned} \tag{72}$$

The Fokker–Planck equation, which is the material time derivative $\dot{p} = dp/dt$, can now be derived from $p = \phi/f$ and Eq. (72) as:

$$\begin{aligned} \frac{dp}{dt} &= -\boldsymbol{\ell} : \nabla(p\boldsymbol{r}) + \frac{1}{f}\xi_c - \frac{1}{f}\xi_l - \frac{\dot{f}}{f}p \\ &= -\boldsymbol{\ell} : \left(\frac{\partial}{\partial\boldsymbol{r}}\otimes(p\boldsymbol{r})\right) + \frac{1}{f}\xi_c - \frac{1}{f}\xi_l - \frac{\dot{f}}{f}p \end{aligned} \tag{73}$$

The terms ξ_c and ξ_l are given by:

$$\xi_c = k_c(1-f)p_c \quad \text{and} \quad \xi_l = k_l f p \tag{74}$$

Substituting Eq. (74) into Eq. (73), we get:

$$\begin{aligned} \dot{p} &= -\boldsymbol{\ell}:\left(\frac{\partial}{\partial\boldsymbol{r}}\otimes(p\boldsymbol{r})\right) - k_c\left(1-\frac{1}{f}\right)p_c \\ &\quad - k_l p - \frac{\dot{f}}{f}p \end{aligned} \tag{75}$$

As can be seen from above, p evolves under (1.) spatial velocity gradient and (2.) topological transitions. The rate $\dot{f}$ can be derived using Eqs. (72) and (74) as:

$$\begin{aligned}\dot{f} &= \int_\Omega \frac{d\phi}{dt}\, d\Omega \\ &= k_c(1-f) - f\int_\Omega k_l p\, d\Omega \\ &= k_c(1-f) - k_l f\end{aligned} \tag{76}$$

Note that above we have assumed that k_l is independent of $\boldsymbol{r}$.

(f) Derivation for $\boldsymbol{\mu}_T$. For T1 transitions, we have the following governing equation:

$$\dot{\boldsymbol{\mu}} = \boldsymbol{\ell}\boldsymbol{\mu} + \boldsymbol{\mu}\boldsymbol{\ell}^T - k_T(\boldsymbol{\mu} - \boldsymbol{\mu}_T)$$

Pre-multiplying the above equation and then taking its Trace, we get:

$$\begin{aligned}\mathrm{Tr}\,(\boldsymbol{\mu}^{-1}\dot{\boldsymbol{\mu}}) &= \mathrm{Tr}\,(\boldsymbol{\mu}^{-1}\boldsymbol{\ell}\boldsymbol{\mu}) + \mathrm{Tr}\,(\boldsymbol{\ell}^T) \\ &\quad - k_T\big(\mathrm{Tr}\,(\boldsymbol{I}) - \mathrm{Tr}\,(\boldsymbol{\mu}^{-1}\boldsymbol{\mu}_T)\big)\end{aligned} \tag{77}$$

Applying Jacobi's formula on the LHS term, which gives $\mathrm{Tr}\,(\boldsymbol{\mu}^{-1}\dot{\boldsymbol{\mu}}) = 2\dot{J}_e/J_e$, and recognizing $\mathrm{Tr}\,(\boldsymbol{\mu}^{-1}\boldsymbol{\ell}\boldsymbol{\mu}) = \mathrm{Tr}\,(\boldsymbol{\ell}) = \mathrm{Tr}\,(\boldsymbol{\ell}^T) = \dot{J}/J$, the above equation becomes:

$$2\frac{\dot{J}_e}{J_e} = 2\frac{\dot{J}}{J} - k_T\big(3 - \mathrm{Tr}\,(\boldsymbol{\mu}^{-1}\boldsymbol{\mu}_T)\big) \tag{78}$$

Further employing $J = J_e J_i$, we get:

$$k_T\big(3 - \mathrm{Tr}\,(\boldsymbol{\mu}^{-1}\boldsymbol{\mu}_T)\big) = 2\frac{\dot{J}_i}{J_i} \tag{79}$$

Now, T1 transition is an isochoric inelastic process, i.e., $\dot{J}_i/J_i = 0$. Furthermore, for biased T1 transitions, we have $\boldsymbol{\mu}_T = \mu_T \boldsymbol{I}$ (an isotropic tensor). Substituting these into Eq. (79), we finally obtain:

$$\boldsymbol{\mu}_T = \frac{3}{\mathrm{Tr}\,(\boldsymbol{\mu}^{-1})}\boldsymbol{I}$$

(g) Thermodynamic admissibility for $\boldsymbol{d}_T$. To show that derived constitutive laws for T1 transition ($\boldsymbol{d}_T$) and division ($\boldsymbol{d}_D$) are thermodynamically admissible, we employ the Clausius–Duhem inequality in Eq. (59). Given that the strain-energy density $\psi_n = \psi_n(\boldsymbol{\mu})$, we have (from Eq. (30)):

$$\begin{aligned}\dot{\psi}_n &= 2\frac{\partial\psi_n}{\partial\boldsymbol{\mu}}\boldsymbol{\mu}\!:\!\boldsymbol{\ell} - \frac{\partial\psi_n}{\partial\boldsymbol{\mu}}\!:\!\boldsymbol{d}_E \\ &\quad - \frac{\partial\psi_n}{\partial\boldsymbol{\mu}}\!:\!\boldsymbol{d}_D - \frac{\partial\psi_n}{\partial\boldsymbol{\mu}}\!:\!\boldsymbol{d}_T\end{aligned} \tag{80}$$

Substituting the above into Clausius–Duhem inequality (Eq. (59)) results in:

$$\begin{aligned}\mathscr{D} &= \left(\boldsymbol{\sigma} - \frac{2}{J_e}\frac{\partial\psi_n}{\partial\boldsymbol{\mu}}\boldsymbol{\mu}\right)\!:\!\boldsymbol{\ell} + \frac{1}{J_e}\frac{\partial\psi_n}{\partial\boldsymbol{\mu}}\!:\!\boldsymbol{d}_E \\ &\quad + \underbrace{\frac{1}{J_e}\frac{\partial\psi_n}{\partial\boldsymbol{\mu}}\!:\!\boldsymbol{d}_T}_{\mathscr{D}_T} + \underbrace{\frac{1}{J_e}\frac{\partial\psi_n}{\partial\boldsymbol{\mu}}\!:\!\boldsymbol{d}_D}_{\mathscr{D}_D} + \frac{1}{J_e}\frac{\dot{\rho}_n}{\rho_n}\psi_n \geq 0\end{aligned} \tag{81}$$

In above equation, $\mathscr{D}_T$ and $\mathscr{D}_D$ represent, respectively, dissipation due to T1 transition and division. Let us look at dissipation due to T1 transition given by:

$$\mathscr{D}_T = \frac{1}{J_e}\frac{\partial\psi_n}{\partial\boldsymbol{\mu}} : \boldsymbol{d}_T = \frac{1}{J_e}\mathrm{Tr}\left(\frac{\partial\psi_n}{\partial\boldsymbol{\mu}}\boldsymbol{d}_T^T\right) \tag{82}$$

Identifying from Eq (40) that $\boldsymbol{d}_T$ is symmetric (i.e., $\boldsymbol{d}_T^T = \boldsymbol{d}_T$), we can write:

$$\begin{aligned}\mathscr{D}_T &= \frac{1}{J_e}\mathrm{Tr}\left(\frac{\partial\psi_n}{\partial\boldsymbol{\mu}}\boldsymbol{d}_T\right) \\ &= \frac{1}{J_e}\mathrm{Tr}\left[\left(\frac{\partial\psi_n}{\partial I_1}\boldsymbol{I} + \frac{\partial\psi_n}{\partial I_3}I_3\boldsymbol{\mu}^{-1}\right)\boldsymbol{d}_T\right] \\ &= \frac{1}{J_e}\left[\frac{\partial\psi_n}{\partial I_1}\mathrm{Tr}\,(\boldsymbol{d}_T) + \frac{\partial\psi_n}{\partial I_3}I_3\,\mathrm{Tr}\,(\boldsymbol{\mu}^{-1}\boldsymbol{d}_T)\right]\end{aligned}$$

In above equation, $I_1 = \mathrm{Tr}\,(\boldsymbol{\mu})$ and $I_3 = \det\boldsymbol{\mu}$ are first and thirds invariants, respectively, of $\boldsymbol{\mu}$ and we have used the fact that ψ_n does not depend on the second invariant I_2 (i.e., $\partial\psi_n/\partial I_2 = 0$). Further substituting $\boldsymbol{d}_T$ from Eq. 40 into above gives:

$$\mathscr{D}_T = \frac{k_T}{J_e}\frac{\partial\psi_n}{\partial I_1}\mathrm{Tr}\,(\boldsymbol{\mu} - \boldsymbol{\mu}_T) \tag{83}$$

Now, k_T, J_e and $\partial\psi_n/\partial I_1$ are all ≥ 0. For $\mathscr{D}_T \geq 0$ to be true, the remaining term must satisfy $\mathrm{Tr}\,(\boldsymbol{\mu} - \boldsymbol{\mu}_T) \geq 0$. Using $\boldsymbol{\mu}_T$ from Eq. (39) for biased T1 transition, we now need to show:

$$\mathrm{Tr}\,(\boldsymbol{\mu})\,\mathrm{Tr}\,(\boldsymbol{\mu}^{-1}) \geq 9 \tag{84}$$

Let $\boldsymbol{\mu} = \mathrm{Diag}\{a, b, c\}$ in principal coordinates, where a, b, c are eigenvalues of tensor $\boldsymbol{\mu}$. Since we are dealing with invariants, the choice of the coordinate system does not matter. Using this diagonalized form of tensor $\boldsymbol{\mu}$ in above inequality, we get:

$$(a+b+c)\left(\frac{1}{a} + \frac{1}{b} + \frac{1}{c}\right) \geq 9 \tag{85}$$

which is satisfied for all $a > 0, b > 0, c > 0$.

(h) Derivation for $\boldsymbol{\mu}_D$. Using Eq. (20), the $\mathcal{L}(\boldsymbol{\mu})$ (Eq. (27)) for division can be written as:

$$\begin{aligned}\mathcal{L}(\boldsymbol{\mu}) &= -k_c\left(1-\frac{1}{f}\right)\frac{\boldsymbol{M}_c}{m_n} - k_l\boldsymbol{\mu} - \frac{\dot{f}}{f}\boldsymbol{\mu} - \frac{\dot{m}_n}{m_n}\boldsymbol{\mu}\\ &= -k_c\left(1-\frac{1}{f}\right)\boldsymbol{\mu}_D - k_D\boldsymbol{\mu} - k_D\boldsymbol{\mu} - \frac{2}{3}\frac{\dot{\zeta}_i}{\zeta_i}\boldsymbol{\mu}\\ &= 2k_D\boldsymbol{\mu}_D - 2k_D\boldsymbol{\mu} + \frac{2}{3}k_D\boldsymbol{\mu}\\ &= k_D\left(2\boldsymbol{\mu}_D - \frac{4}{3}\boldsymbol{\mu}\right)\end{aligned} \tag{86}$$

Therefore for division, we have the following governing equation:

$$\dot{\boldsymbol{\mu}} = \boldsymbol{\ell}\boldsymbol{\mu} + \boldsymbol{\mu}\boldsymbol{\ell}^T - k_D\left(\frac{4}{3}\boldsymbol{\mu} - 2\boldsymbol{\mu}_D\right)$$

Following the similar steps as for T1 transitions in Appendix Af, we get:

$$k_D\left(4 - 2\,\mathrm{Tr}\left(\boldsymbol{\mu}^{-1}\boldsymbol{\mu}_D\right)\right) = 2\frac{\dot{J}_i}{J_i} \tag{87}$$

Since the division process is inelastic and isochoric, the RHS of the above equation vanishes and gives:

$$k_D\left(4 - 2\,\mathrm{Tr}\left(\boldsymbol{\mu}^{-1}\boldsymbol{\mu}_D\right)\right) = 0 \tag{88}$$

For oriented/biased divisions $\boldsymbol{\mu}_D = \mu_D\boldsymbol{I}$ is an isotropic tensor. From the above equation, we can obtain:

$$\boldsymbol{\mu}_D = \frac{2}{\mathrm{Tr}\,(\boldsymbol{\mu}^{-1})}\boldsymbol{I}$$

(i) Thermodynamic admissibility for $\boldsymbol{d}_D$. Following the similar steps for T1 transition in Appendix Ag, the dissipation $\mathscr{D}_D$ due to division can be found as:

$$\mathscr{D}_D = \frac{k_D}{J_e}\frac{\partial\psi_n}{\partial I_1}\,\mathrm{Tr}\left(\frac{4}{3}\boldsymbol{\mu} - 2\boldsymbol{\mu}_D\right) \tag{89}$$

Substituting $\boldsymbol{\mu}_D$ from Eq. (48) for biased division, the inequality $\mathscr{D}_D \geq 0$ becomes:

$$\mathrm{Tr}\,(\boldsymbol{\mu})\,\mathrm{Tr}\,(\boldsymbol{\mu}^{-1}) \geq 9 \tag{90}$$

which has been proved already (see Appendix Ag).

Acknowledgements FJV gratefully acknowledges the support of the National Science Foundation, USA, under Award No. 2135057. The content is solely the responsibility of the authors and does not necessarily represent the official views of the National Science Foundation.

References

Ambrosi D, Ateshian G, Arruda E, Cowin S, Dumais J, Goriely A, Holzapfel G, Humphrey J, Kemkemer R, Kuhl E, Olberding J, Taber L, Garikipati K (2011) Perspectives on biological growth and remodeling. J Mech Phys Solids 59(4):863–883. https://doi.org/10.1016/j.jmps.2010.12.011

Ambrosi D, Mollica F (2002) On the mechanics of a growing tumor. Int J Eng Eng Sci 40(12):1297–1316. https://doi.org/10.1016/S0020-7225(02)00014-9

Ambrosi D, Mollica F (2004) The role of stress in the growth of a multicell spheroid. J Math Biol 48(5):477–499. https://doi.org/10.1007/s00285-003-0238-2

Ambrosi D, Preziosi L (2009) Cell adhesion mechanisms and stress relaxation in the mechanics of tumours. Biomech Model Mechanobiol 8(5):397–413

Ateshian GA, Morrison B, Holmes JW, Hung CT (2012) Mechanics of cell growth. Mech Res Commun 42:118–125. https://doi.org/10.1016/j.mechrescom.2012.01.010

Aubouy M, Jiang Y, Glazier JA, Graner F (2003) A texture tensor to quantify deformations. Granular Matter 5(2):67–70. https://doi.org/10.1007/s10035-003-0126-x

Bandil P, Vernerey FJ (2023) Continuum theory for confluent cell monolayers: interplay between cell growth, division, and intercalation. J Mech Phys Solids 181:105443. https://doi.org/10.1016/j.jmps.2023.105443

Barton DL, Henkes S, Weijer CJ, Sknepnek R (2017) Active Vertex Model for cell-resolution description of epithelial tissue mechanics. PLoS Comput Biol 13(6):e1005569. https://doi.org/10.1371/journal.pcbi.1005569

Brodland G, Chen D, Veldhuis J (2006) A cell-based constitutive model for embryonic epithelia and other planar aggregates of biological cells. Int J Plast 22(6):965–995. https://doi.org/10.1016/j.ijplas.2005.05.002

Cheng G, Tse J, Jain RK, Munn LL (2009) Micro-environmental mechanical stress controls tumor spheroid size and morphology by suppressing proliferation and inducing apoptosis in cancer cells. PLoS ONE 4(2):e4632. https://doi.org/10.1371/journal.pone.0004632

Crespo-Cuevas V, Ferguson VL, Vernerey F (2023) Poroviscoelasto–plasticity of agarose-based hydrogels. Soft Matter 19(4):790–806. https://doi.org/10.1039/D2SM01356H

Dhote V, Vernerey FJ (2014) Mathematical model of the role of degradation on matrix development in hydrogel scaffold. Biomech Model Mechanobiol 13(1):167–183. https://doi.org/10.1007/s10237-013-0493-0

Farhadifar R, Röper J-C, Aigouy B, Eaton S, Jülicher F (2007) The influence of cell mechanics, cell-cell interactions, and proliferation on epithelial packing. Curr Biol 17(24):2095–2104. https://doi.org/10.1016/j.cub.2007.11.049

Garikipati K (2009) The kinematics of biological growth. Appl Mech Rev 62(3):030801. https://doi.org/10.1115/1.3090829

Gillies TE, Cabernard C (2011) Cell division orientation in animals. Curr Biol 21(15):R599–R609. https://doi.org/10.1016/j.cub.2011.06.055

Goriely A (2017) The Mathematics and Mechanics of Biological Growth (Vol. 45). Springer New York. https://doi.org/10.1007/978-0-387-87710-5

Graner F, Dollet B, Raufaste C, Marmottant P (2008) Discrete rearranging disordered patterns, part I: robust statistical tools in two or three dimensions. Eur Phys J E 25(4):349–369. https://doi.org/10.1140/epje/i2007-10298-8

Holzapfel GA (2000) Nonlinear solid mechanics: a continuum approach for engineering. Wiley

Holzapfel GA, Gasser TC, Ogden RW (2004) A new constitutive framework for arterial wall mechanics and a comparative study of material models. In Cowin SC and Humphrey JD (Eds), Cardiovascular Soft Tissue Mechanics (pp 1–48). Kluwer Academic Publishers.

Huang R, Ogden RW, Penta R (2021) Mathematical modelling of residual-stress based volumetric growth in soft matter. J Elast 145(1–2):223–241. https://doi.org/10.1007/s10659-021-09834-8

Ishihara S, Marcq P, Sugimura K (2017) From cells to tissue: a continuum model of epithelial mechanics. Phys Rev E 96(2):022418. https://doi.org/10.1103/PhysRevE.96.022418

Jones GW, Chapman SJ (2012) Modeling growth in biological materials. SIAM Rev 54(1):52–118. https://doi.org/10.1137/080731785
Kao PH, Lammers SR, Tian L, Hunter K, Stenmark KR, Shandas R, Qi HJ (2011) A microstructurally driven model for pulmonary artery tissue. J Biomech Eng 133(5):051002. https://doi.org/10.1115/1.4002698
Keller R, Davidson L, Edlund A, Elul T, Ezin M, Shook D, Skoglund P (2000) Mechanisms of convergence and extension by cell intercalation. Phil Trans R Soc Lond B 355(1399):897–922. https://doi.org/10.1098/rstb.2000.0626
Kuhl E (2014) Growing matter: a review of growth in living systems. J Mech Behav Biomed Mater 29:529–543. https://doi.org/10.1016/j.jmbbm.2013.10.009
Kulwatno J, Gearhart J, Gong X, Herzog N, Getzin M, Skobe M, Mills KL (2021) Growth of tumor emboli within a vessel model reveals dependence on the magnitude of mechanical constraint. Integr Biol 13(1):1–16. https://doi.org/10.1093/intbio/zyaa024
Lalitha Sridhar S, Ortega JK, Vernerey FJ (2018) A statistical model of expansive growth in plant and fungal cells: the case of phycomyces. Biophys J 115(12):2428–2442. https://doi.org/10.1016/j.bpj.2018.11.014
Lejeune E, Linder C (2017) Modeling tumor growth with peridynamics. Biomech Model Mechanobiol 16(4):1141–1157. https://doi.org/10.1007/s10237-017-0876-8
Lin S-Z, Li B, Feng X-Q (2017) A dynamic cellular vertex model of growing epithelial tissues. Acta Mech Sin 33(2):250–259. https://doi.org/10.1007/s10409-017-0654-y
Lubarda V, Hoger A (2002) On the mechanics of solids with a growing mass. Int J Solids Struct 39(18):4627–4664. https://doi.org/10.1016/S0020-7683(02)00352-9
Marmottant P, Mgharbel A, Käfer J, Audren B, Rieu J-P, Vial J-C, van der Sanden B, Marée AFM, Graner F, Delanoë-Ayari H (2009) The role of fluctuations and stress on the effective viscosity of cell aggregates. Proc Natl Acad Sci USA 106(41):17271–17275. https://doi.org/10.1073/pnas.0902085106
Mills KL, Kemkemer R, Rudraraju S, Garikipati K (2014) Elastic free energy drives the shape of prevascular solid tumors. PLoS ONE 9(7):e103245. https://doi.org/10.1371/journal.pone.0103245
Montel F, Delarue M, Elgeti J, Vignjevic D, Cappello G, Prost J (2012) Isotropic stress reduces cell proliferation in tumor spheroids. New J Phys 14(5):055008. https://doi.org/10.1088/1367-2630/14/5/055008
Preziosi L, Ambrosi D, Verdier C (2010) An elasto-visco-plastic model of cell aggregates. J Theor Biol 262(1):35–47. https://doi.org/10.1016/j.jtbi.2009.08.023
Rajagopal K (1995) Multiple configurations in continuum mechanics. Reports of the institute for computational and applied mechanics, 6
Rodriguez EK, Hoger A, McCulloch AD (1994) Stress-dependent finite growth in soft elastic tissues. J Biomech 27(4):455–467. https://doi.org/10.1016/0021-9290(94)90021-3
Skalak R, Zargaryan S, Jain RK, Netti PA, Hoger A (1996) Compatibility and the genesis of residual stress by volumetric growth. J Math Biol 34:889–914
Staddon MF, Hernandez A, Bowick MJ, Moshe M, Marchetti MC (2023) The role of non-affine deformations in the elastic behavior of the cellular vertex model. Soft Matter 19(17):3080–3091. https://doi.org/10.1039/D2SM01580C
Taber LA (2020) Continuum Modeling in Mechanobiology. Springer International Publishing. https://doi.org/10.1007/978-3-030-43209-6
Tzur A, Kafri R, LeBleu VS, Lahav G, Kirschner MW (2009) Cell growth and size homeostasis in proliferating animal cells. Science 325(5937):167–171. https://doi.org/10.1126/science.1174294
Van Liedekerke P, Palm MM, Jagiella N, Drasdo D (2015) Simulating tissue mechanics with agent-based models: concepts, perspectives and some novel results. Comput Part Mech 2(4):401–444. https://doi.org/10.1007/s40571-015-0082-3
Vernerey FJ (2016) A mixture approach to investigate interstitial growth in engineering scaffolds. Biomech Model Mechanobiol 15(2):259–278. https://doi.org/10.1007/s10237-015-0684-y
Vernerey FJ, Lalitha Sridhar S, Muralidharan A, Bryant SJ (2021) Mechanics of 3D cell-hydrogel interactions: experiments, models, and mechanisms. Chem Rev 121(18):11085–11148. https://doi.org/10.1021/acs.chemrev.1c00046
Vernerey FJ, Long R, Brighenti R (2017) A statistically-based continuum theory for polymers with transient networks. J Mech Phys Solids 107:1–20. https://doi.org/10.1016/j.jmps.2017.05.016
Vernerey FJ, Shen T, Sridhar SL, Wagner RJ (2018) How do fire ants control the rheology of their aggregations? a statistical mechanics approach. J R Soc Interf 15(147):20180642. https://doi.org/10.1098/rsif.2018.0642
Wyatt TPJ, Harris AR, Lam M, Cheng Q, Bellis J, Dimitracopoulos A, Kabla AJ, Charras GT, Baum B (2015) Emergence of homeostatic epithelial packing and stress dissipation through divisions oriented along the long cell axis. Proc Natl Acad Sci 112(18):5726–5731. https://doi.org/10.1073/pnas.1420585112
Xu G-K, Liu Y, Li B (2015) How do changes at the cell level affect the mechanical properties of epithelial monolayers? Soft Matter 11(45):8782–8788. https://doi.org/10.1039/C5SM01966D
Xu G-K, Liu Y, Zheng Z (2016) Oriented cell division affects the global stress and cell packing geometry of a monolayer under stretch. J Biomech 49(3):401–407. https://doi.org/10.1016/j.jbiomech.2015.12.046
Yan H, Ramirez-Guerrero D, Lowengrub J, Wu M (2021) Stress generation, relaxation and size control in confined tumor growth. PLOS Comput Biol 17(12):e1009701
Zhang H, Li B, Shao Y, Feng X-Q (2020) Morphomechanics of tumors. Current Opin Biomed Eng 15:51–58. https://doi.org/10.1016/j.cobme.2020.01.004
Zhao Z, Chen X, Dowbaj AM, Sljukic A, Bratlie K, Lin L, Fong ELS, Balachander GM, Chen Z, Soragni A, Huch M, Zeng YA, Wang Q, Yu H (2022) Organoids. Nat Rev Methods Primers 2(1):94. https://doi.org/10.1038/s43586-022-00174-y